

## Supplementary Materials for

# Understanding Fragility and Engineering Activation Stability in Two-Dimensional Covalent Organic Frameworks

Dongyang Zhu,<sup>1†</sup> Jun-Jie Zhang,<sup>2†</sup> Xiaowei Wu,<sup>3,4†</sup> Qianqian Yan,<sup>2</sup> Fangxin Liu,<sup>1</sup> Yifan Zhu,<sup>2</sup> Xiaodong Gao,<sup>5</sup> Muhammad M. Rahman,<sup>2</sup> Boris I. Yakobson,<sup>2,6</sup> Pulickel M. Ajayan<sup>2</sup> and Rafael Verduzco\*<sup>1,2</sup>

1. Department of Chemical and Biomolecular Engineering, Rice University, 6100 Main Street, MS-362, Houston, Texas 77005, United States

2. Department of Materials Science and Nanoengineering, Rice University, 6100 Main Street, MS-325, Houston, Texas 77005, United States

3. CAS Key Laboratory of Design and Assembly of Functional Nanostructures, Fujian Provincial Key Laboratory of Nanomaterials, Fujian Institute of Research on the Structure of Matter (FJIRSM), Chinese Academy of Sciences, Fuzhou 350002, China

4. Xiamen Key Laboratory of Rare Earth Photoelectric Functional Materials, Xiamen Institute of Rare Earth Materials (XMIREM), Haixi Institutes, Chinese Academy of Sciences, Xiamen 361021, China

5. Department of Earth, Environmental, and Planetary Sciences, Rice University, 6100 Main Street, MS-126, Houston, Texas 77005, United States

6. Department of Chemistry, Rice University, 6100 Main Street, MS-60, Houston, Texas 77005, United States

\* Corresponding author: Rafael Verduzco

**Email:** rafaelv@rice.edu

†These authors contributed equally to this work.

## Supplementary Text

### Section 1. Materials, Instrumentation and Methods

**Chemicals.** All chemicals were purchased from commercial sources and used without further purification. 1,3,5-tris(4-aminophenyl)benzene (TAPB), 2,5-dibromoterephthalaldehyde (BrPDA), tetrafluoroterephthalaldehyde (FPDA) and 4,4'-diformylbiphenyl (DFBP) were purchased from Ambeed; [1,1'-biphenyl]-4,4'-diamine (BPDA) or benzidine (BZD), terephthalaldehyde (PDA), 2,5-dimethoxyterephthalaldehyde (OMePDA) and tris(4-Formylphenyl)amine (TFPA) were purchased from Sigma Aldrich. 1,3,5-Tri(4-formylphenyl)benzene (TFPB), benzene-1,3,5-tricarbaldehyde (BTCA), 2,5-dihydroxy-1,4-benzenedicarboxaldehyde (OHPDA), 2,5-dichloroterephthalic dicarboxaldehyde (CIPDA), 1,3,6,8-tetrakis(4-aminophenyl)pyrene (Py), 2',5'-dimethoxy-[1,1':4',1''-terphenyl]-4,4''-dicarbaldehyde (OMe3P), [1,1':4',1''-terphenyl]-4,4''-dicarbaldehyde (3P), 5,10,15,20-tetrakis(4-aminophenyl)porphyrin (TTAPP) and bis(octyloxy)terephthalaldehyde (C8PDA) were purchased from Jilin Chinese Academy of Sciences - Yanshen Technology Co., Ltd. Solvents including anhydrous 1-butanol, 1,4-dichlorobenzene (o-DCB), dioxane and mesitylene were purchased from Sigma Aldrich. All other solvents used in this work were purchased from Fisher Scientific.

## Section 2. Understanding fragility

### 2.1 Pore size series

#### 2.1.1. TAPB-BTCA COF

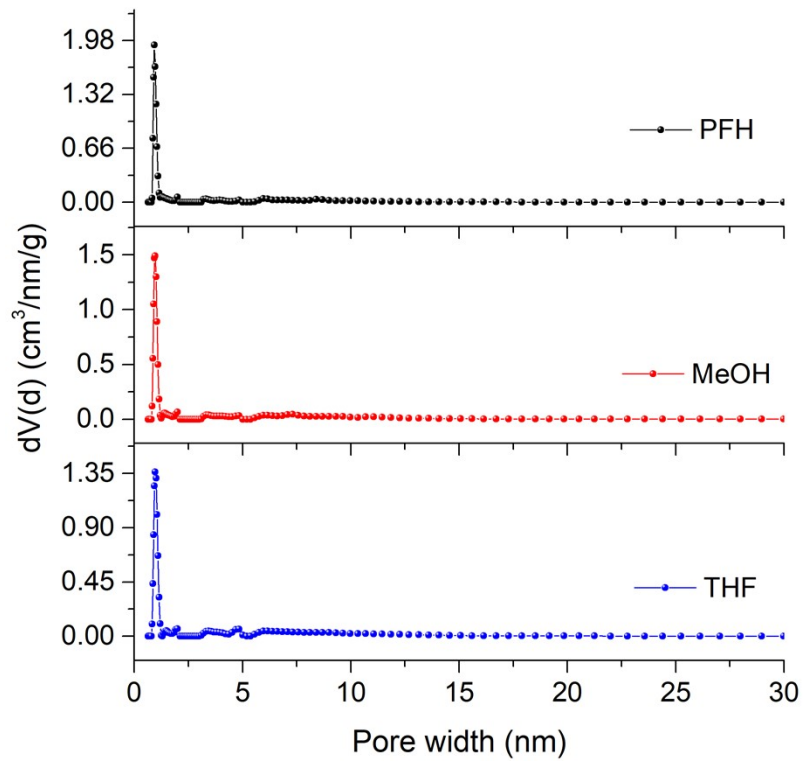


Figure S1. Pore size distributions of TAPB-BTCA COF calculated using QSDFT model.

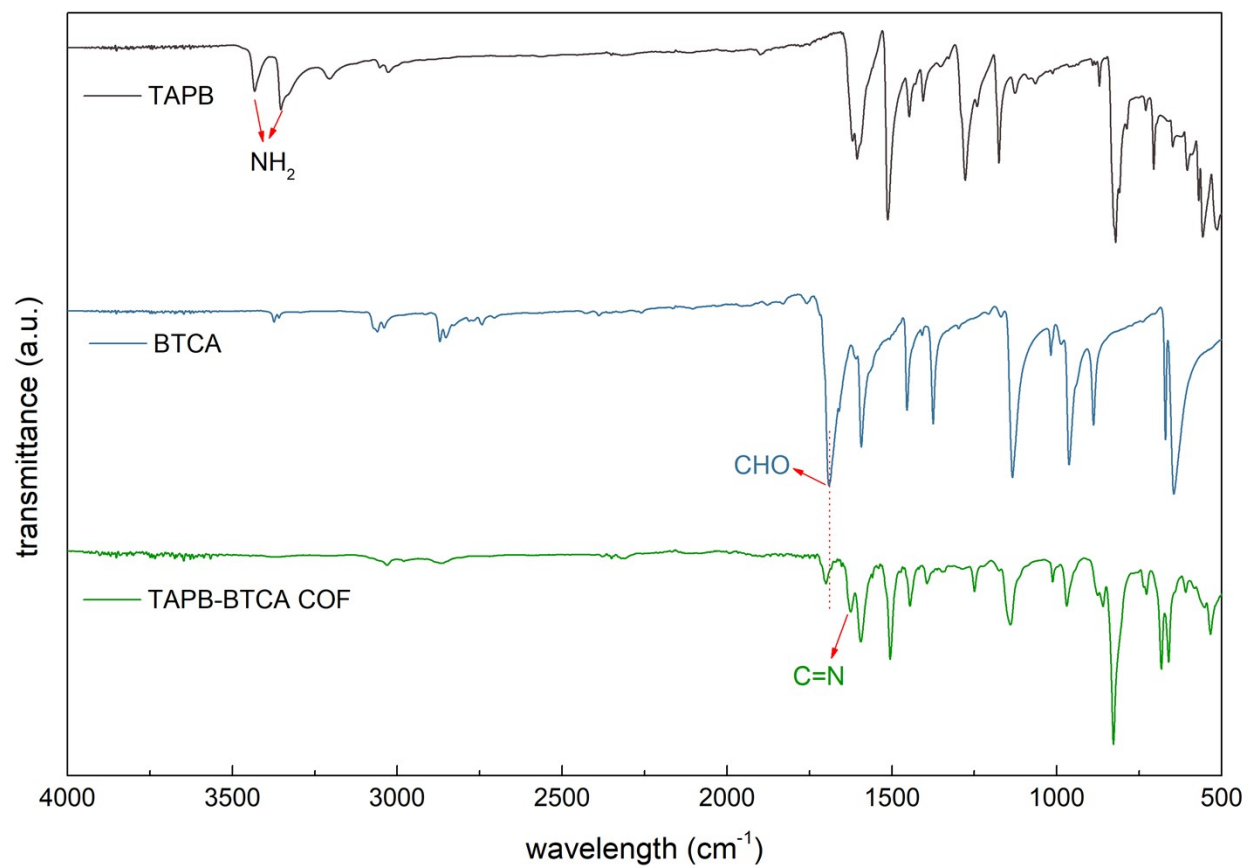


Figure S2. FTIR spectra of TAPB, BTCA monomers and TAPB-BTCA COF.

### 2.1.2. TAPB-TFPB COF

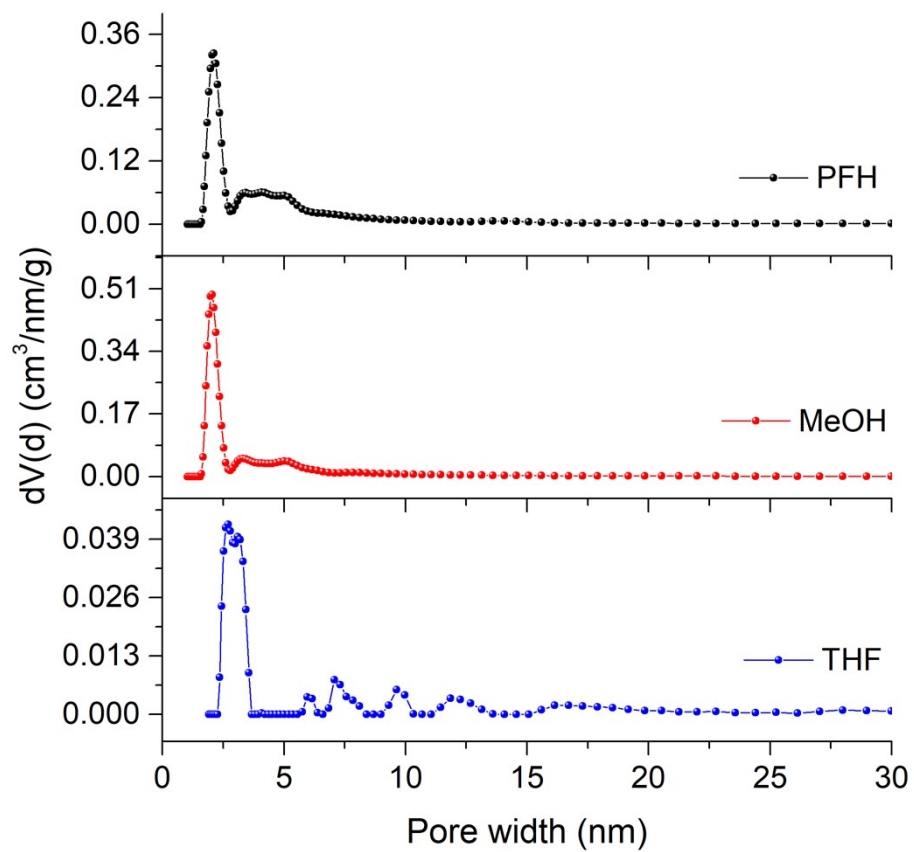


Figure S3. Pore size distributions of TAPB-TFPB COF calculated using QSDFT model.

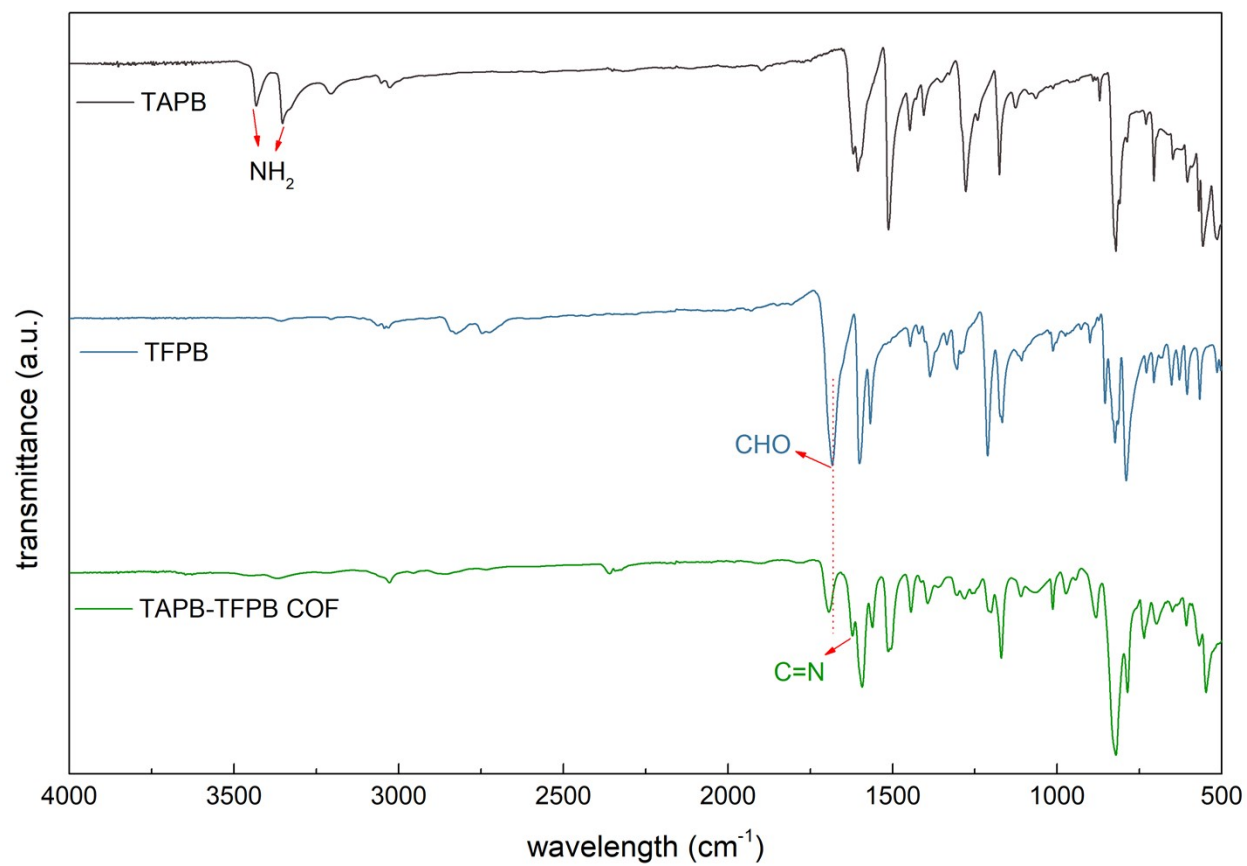


Figure S4. FTIR spectra of TAPB, TFPB monomers and TAPB-TFPB COF.

### 2.1.3. TAPB-PDA COF

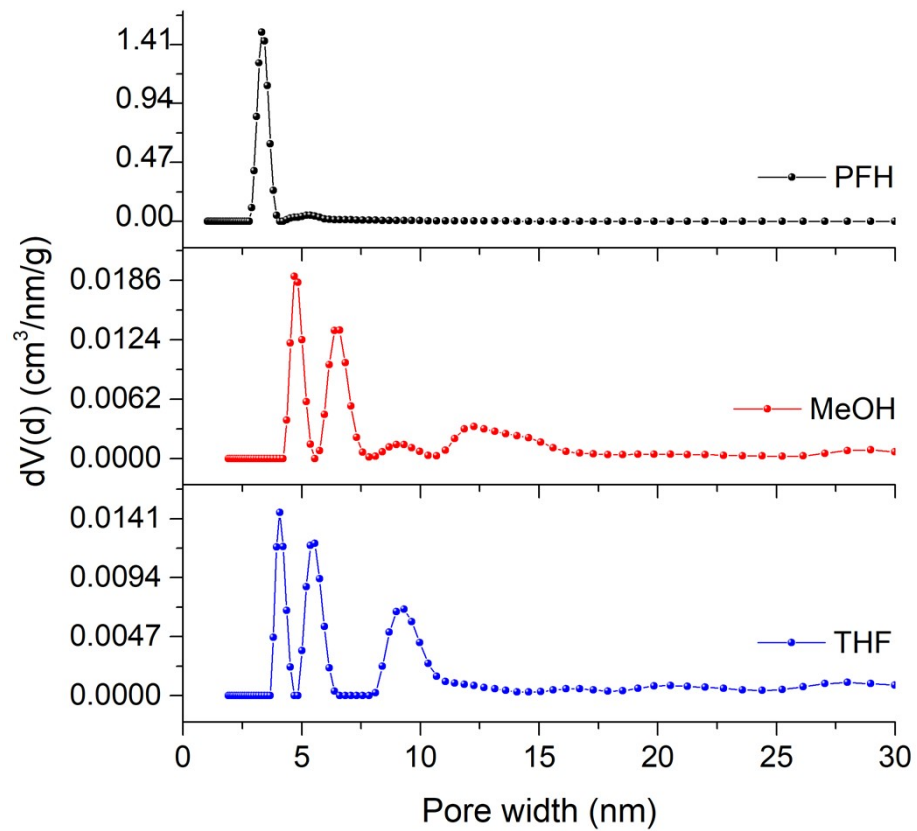


Figure S5. Pore size distributions of TAPB-PDA COF calculated using QSDFT model.

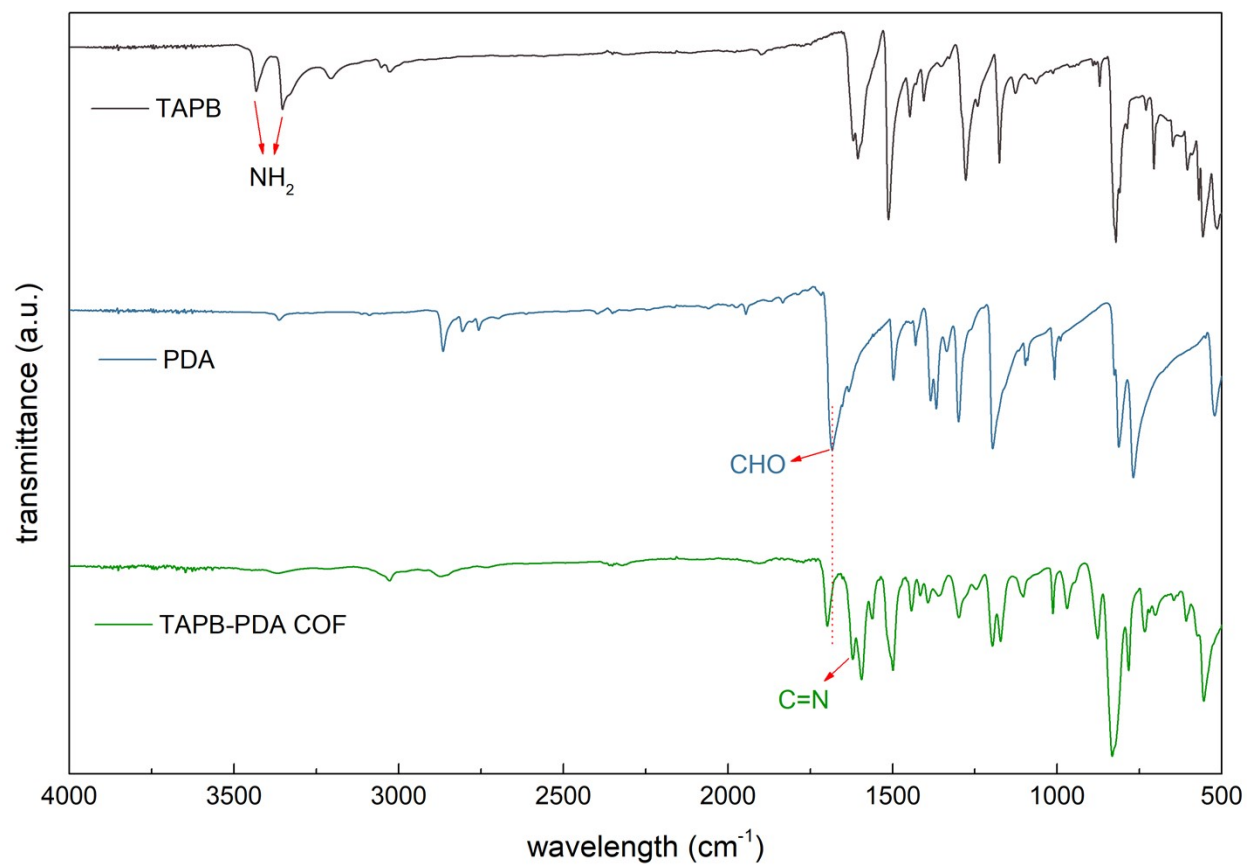


Figure S6. FTIR spectra of TAPB, PDA monomers and TAPB-PDA COF.

#### 2.1.4. TAPB-TFPA COF

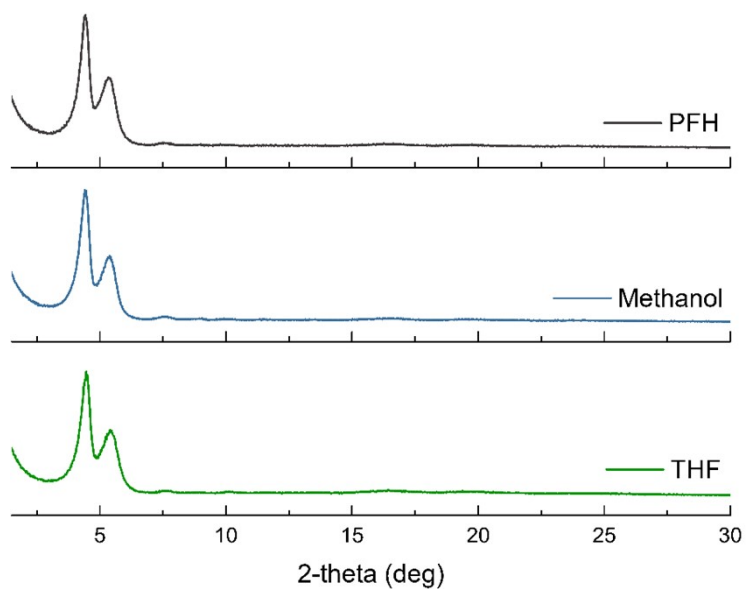


Figure S7. PXRD patterns for TAPB-TFPA COFs after activation using PFH, methanol and THF.

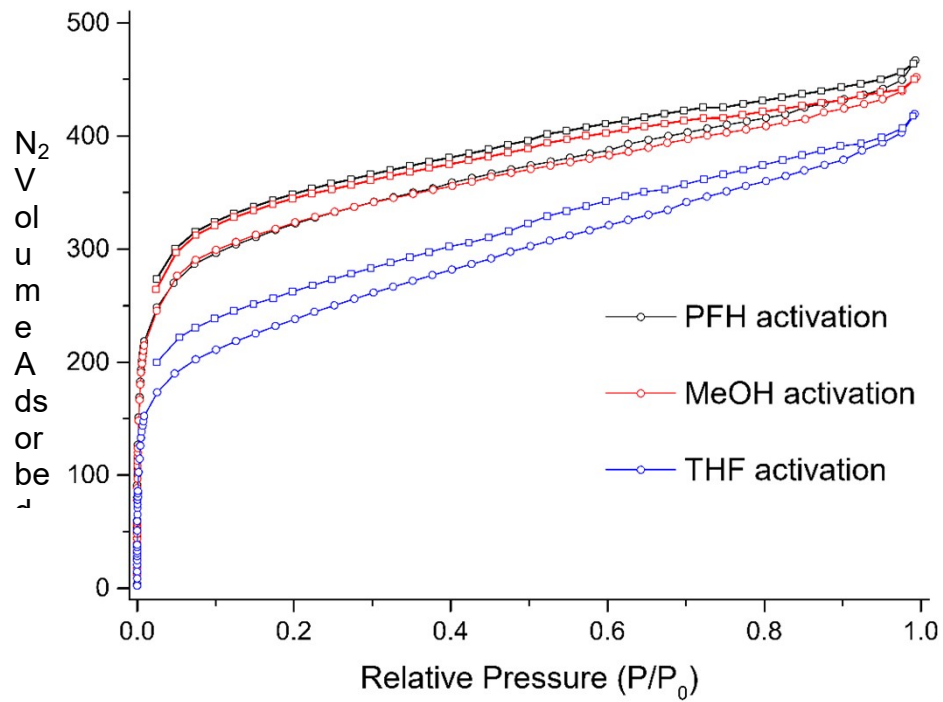


Figure S8. Nitrogen sorption isotherms for TAPB-TFPA COFs after activation using PFH, methanol and THF.

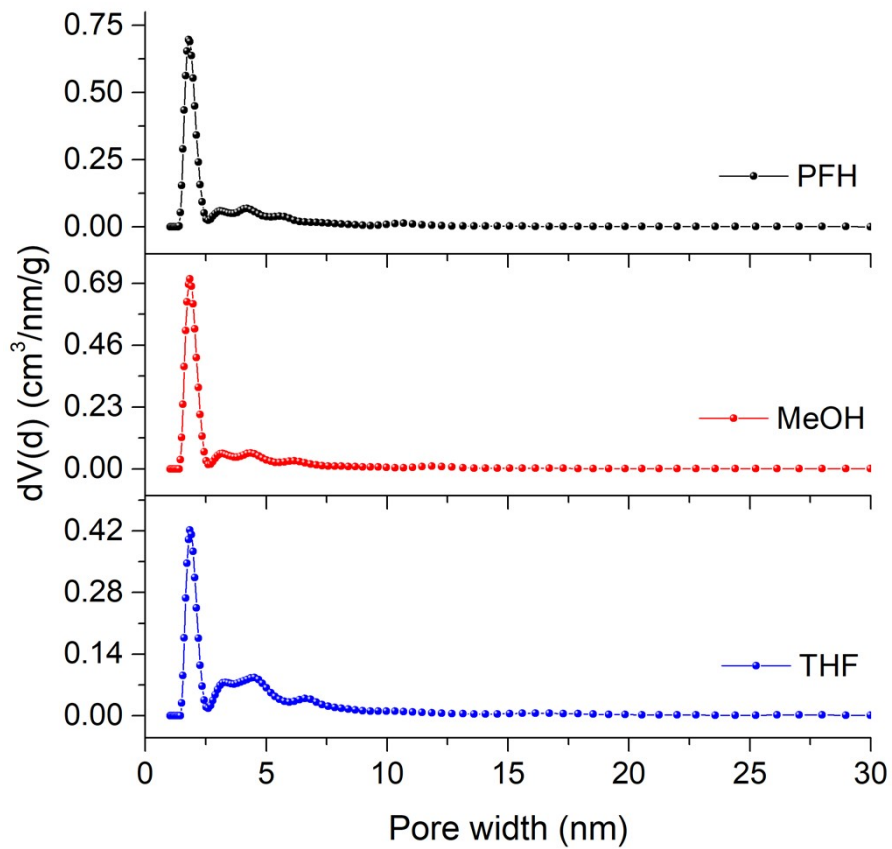


Figure. S9. Pore size distributions of TAPB-TFPA COF calculated using QSDFT model.

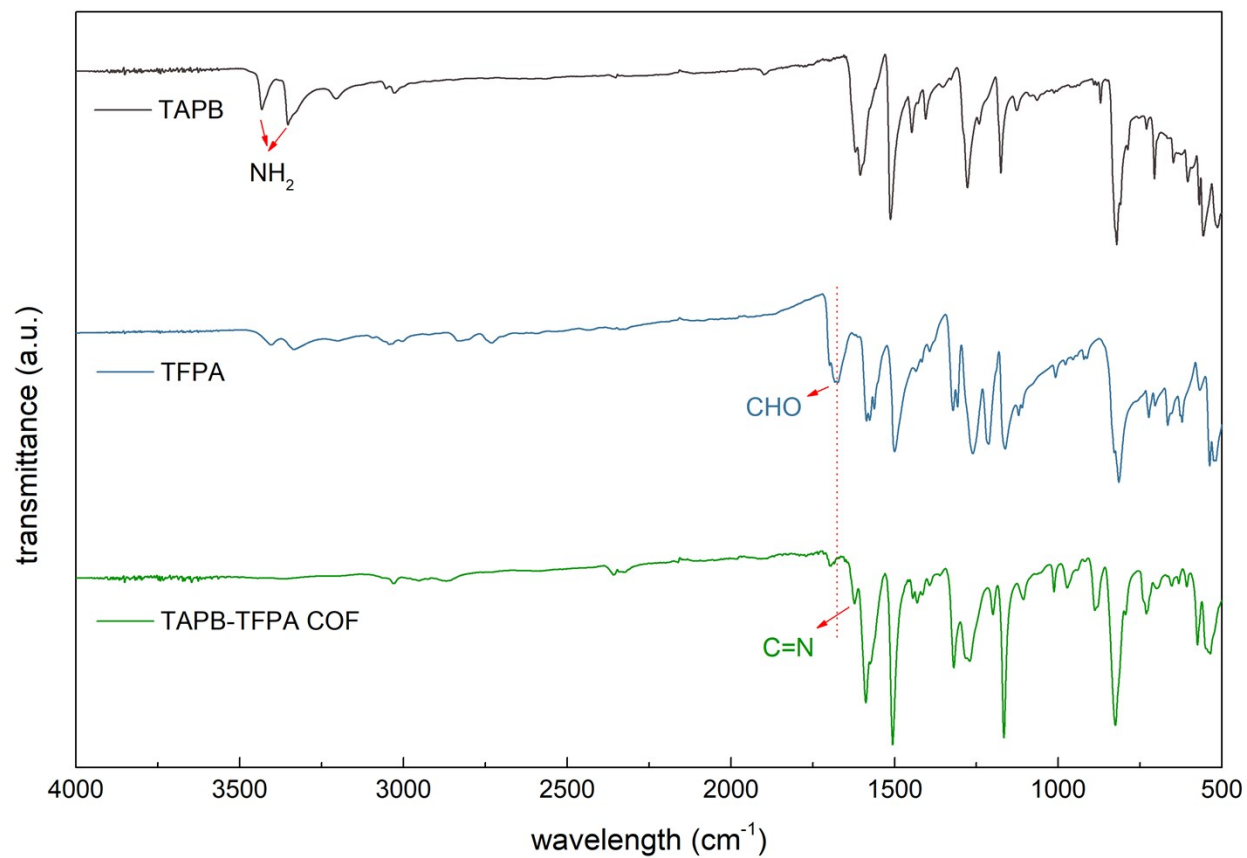


Figure. S10. FTIR spectra of TAPB, TFPA monomers and TAPB-TFPA COF.

### 2.1.5. PI-2 COF

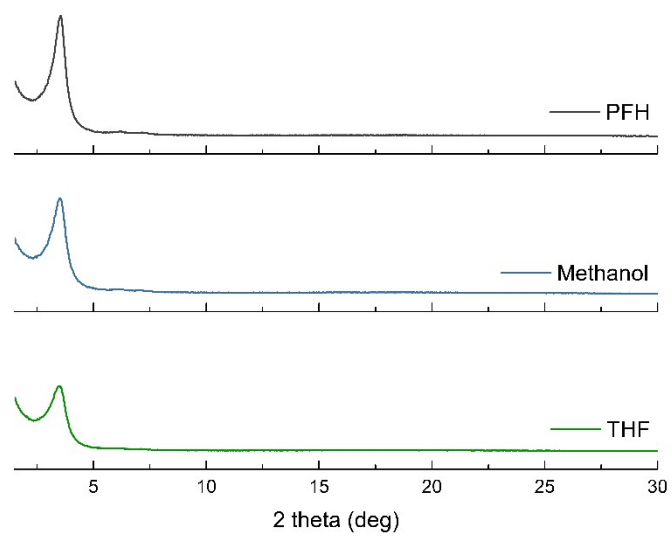


Figure. S11. PXRD patterns for PI-2 COFs after activation using PFH, methanol and THF.

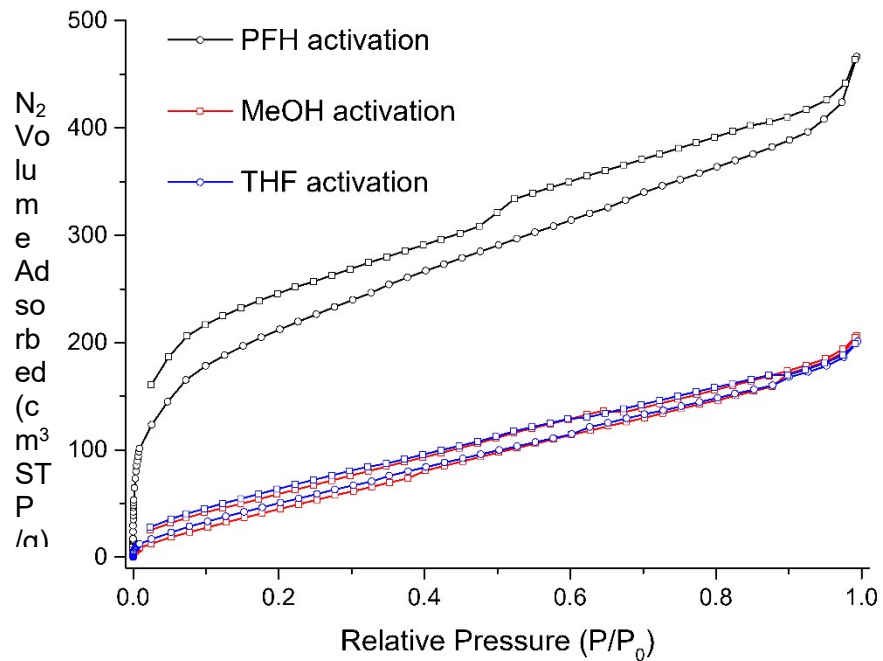


Figure. S12. Nitrogen isotherms for PI-2 COFs after activation using PFH, methanol and THF.

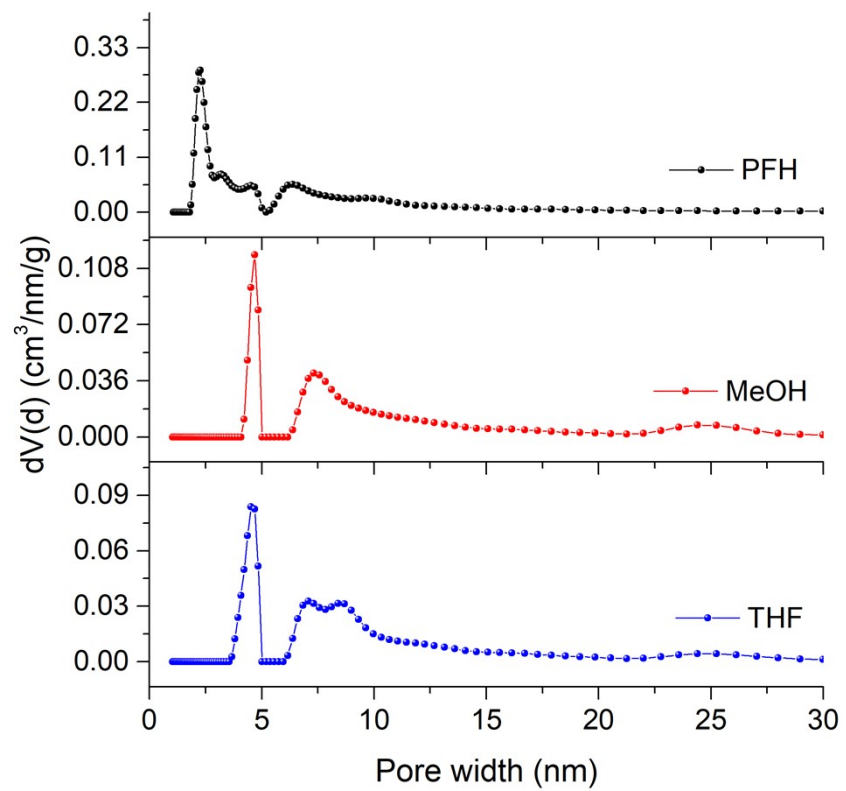


Figure. S13. Pore size distributions of PI-2 COF calculated using QSDFT model.

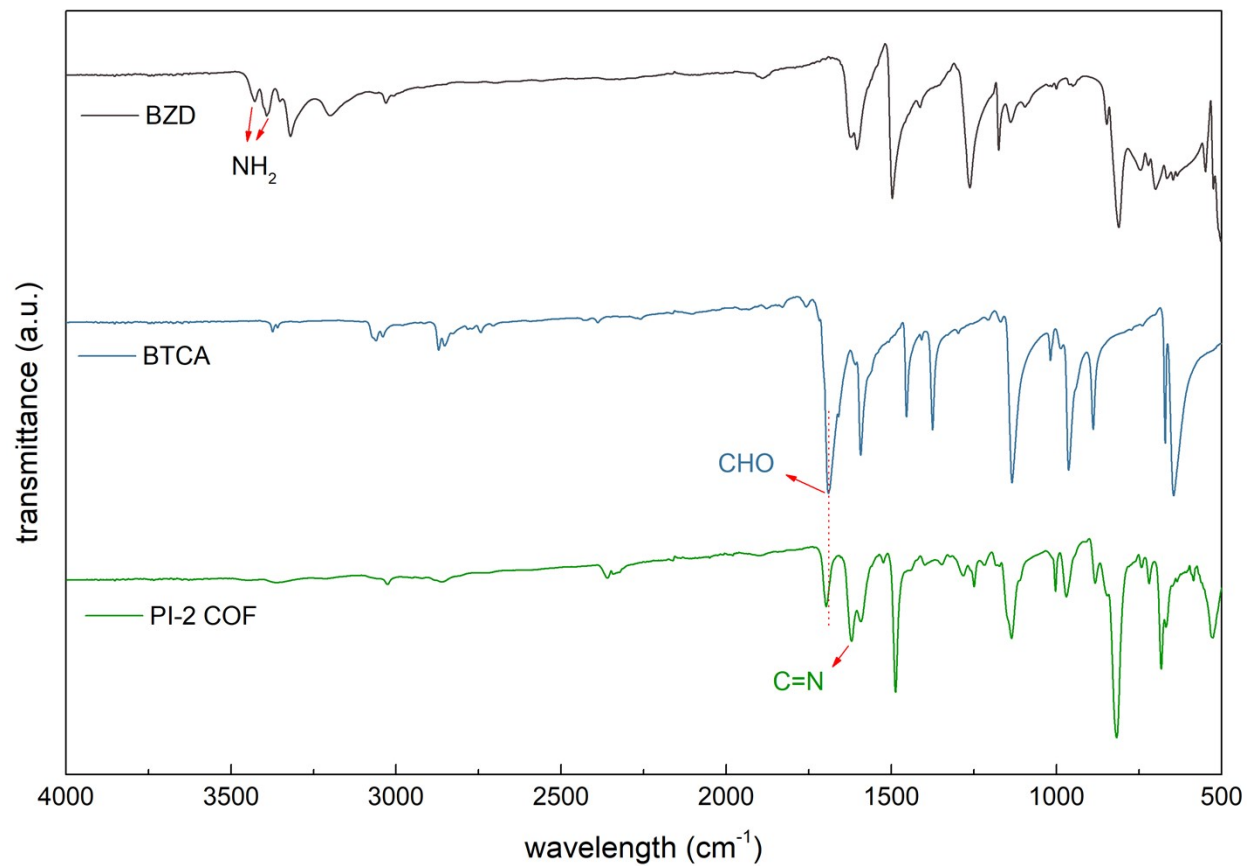


Figure. S14. FTIR spectra of BZD, BTCA monomers and PI-2 COF.

### 2.1.6. Comparison of fragility for COFs with different pore sizes

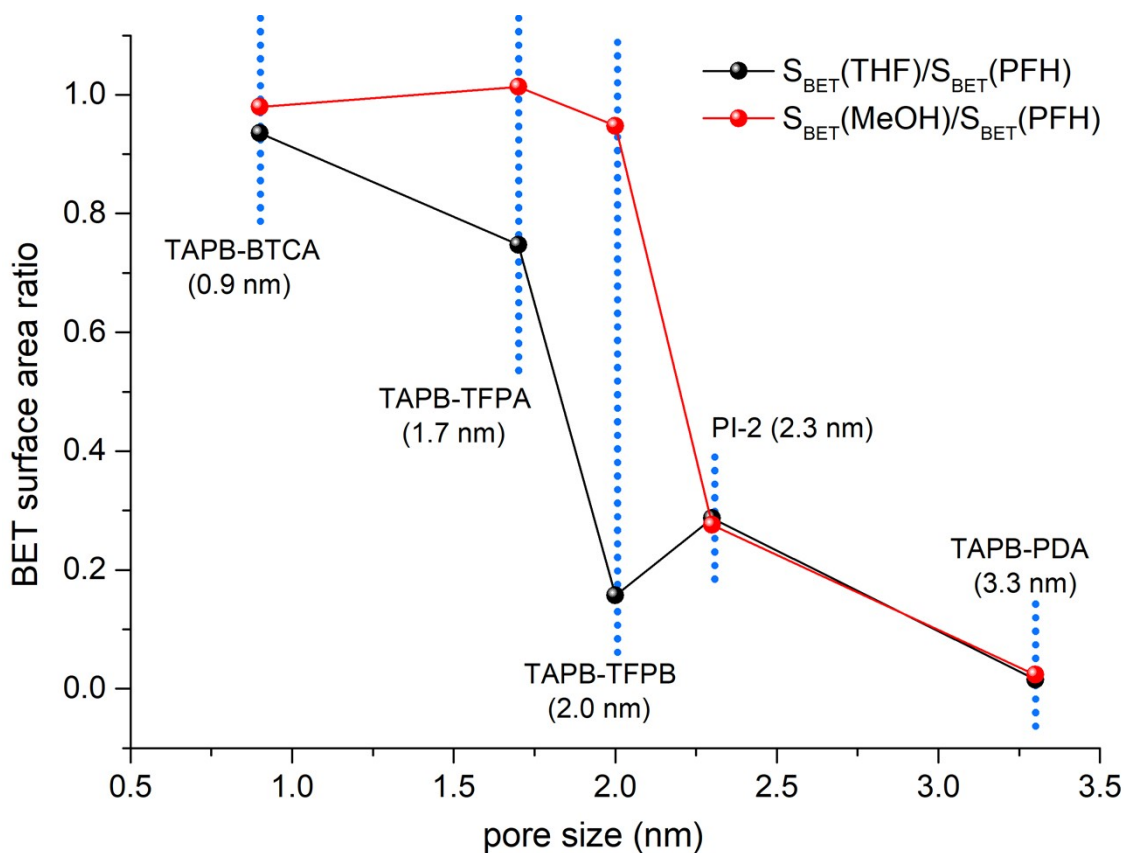


Figure. S15. The ratio of BET surface areas after PFH and THF activation ( $S_{\text{BET}}(\text{THF})/S_{\text{BET}}(\text{PFH})$ ) and those after MeOH and THF activation ( $S_{\text{BET}}(\text{THF})/S_{\text{BET}}(\text{MeOH})$ ).

## 2.2. Pore functionality series

### 2.2.1. TAPB-FPDA COF

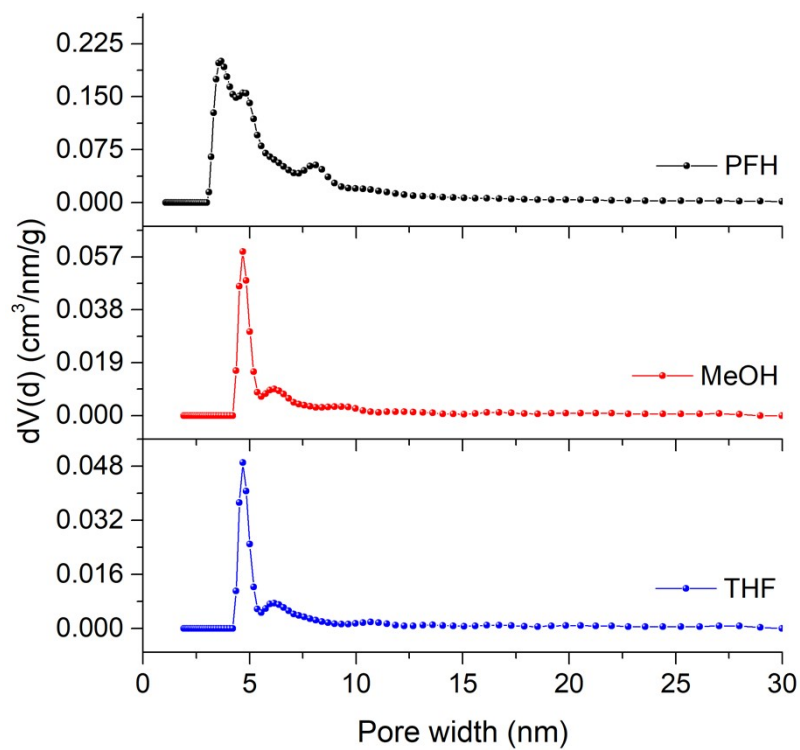


Figure. S16. Pore size distributions of TAPB-FPDA COF calculated using QSDFT model.

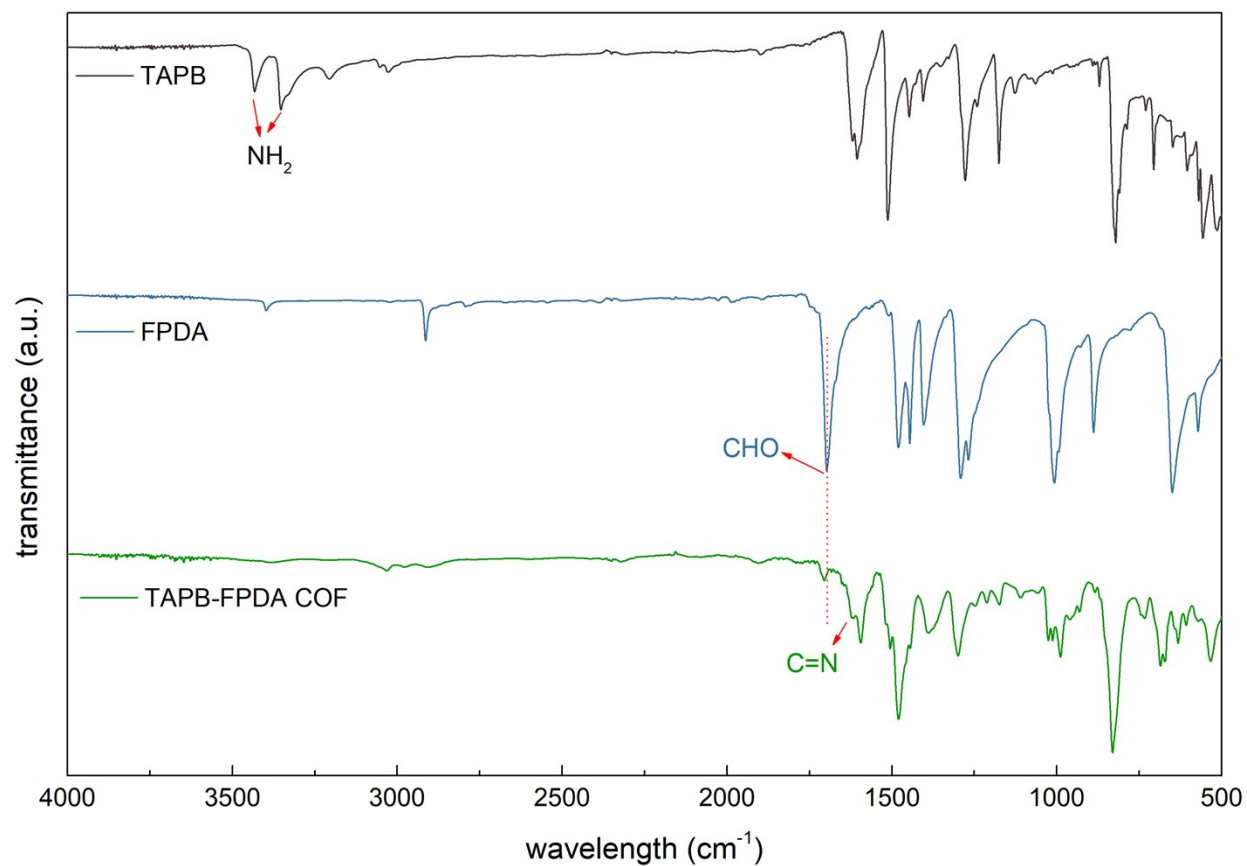


Figure. S17. FTIR spectra of TAPB, FPDA monomers and TAPB-FPDA COF.

### 2.2.2. TAPB-OHPDA COF

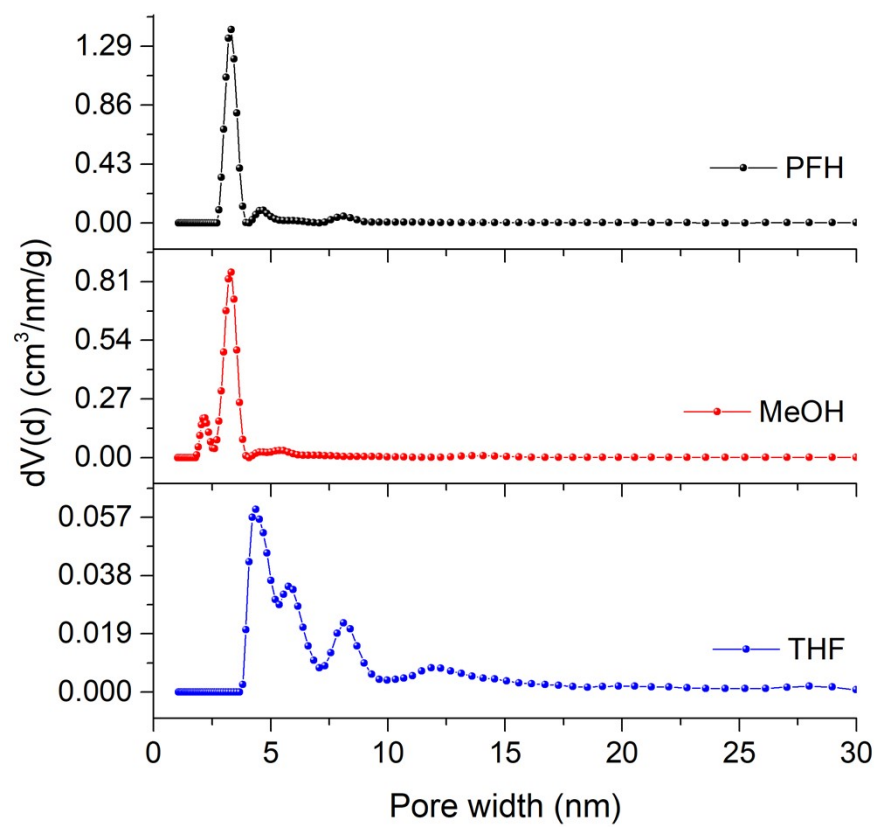


Figure. S18. Pore size distributions of TAPB-OHPDA COF calculated using QSDFT model.

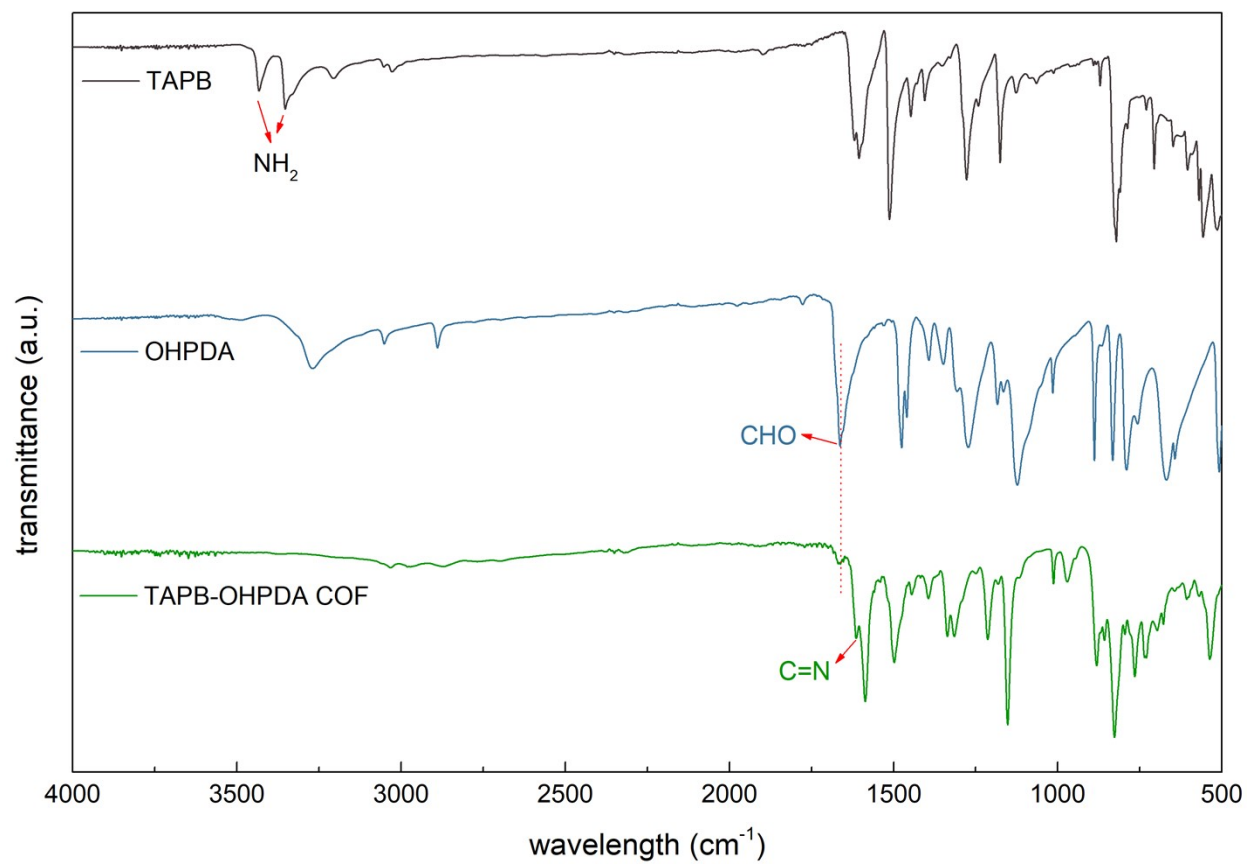


Figure. S19. FTIR spectra of TAPB, OHPDA monomers and TAPB-OHPDA COF.

### 2.2.3. TAPB-CIPDA COF

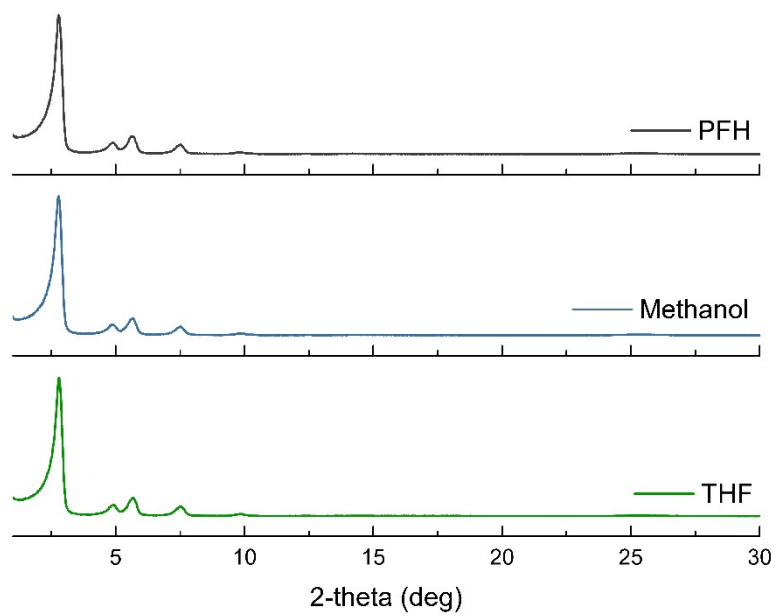


Figure. S20. PXRD patterns for TAPB-CIPDA COFs after activation using PFH, methanol and THF.

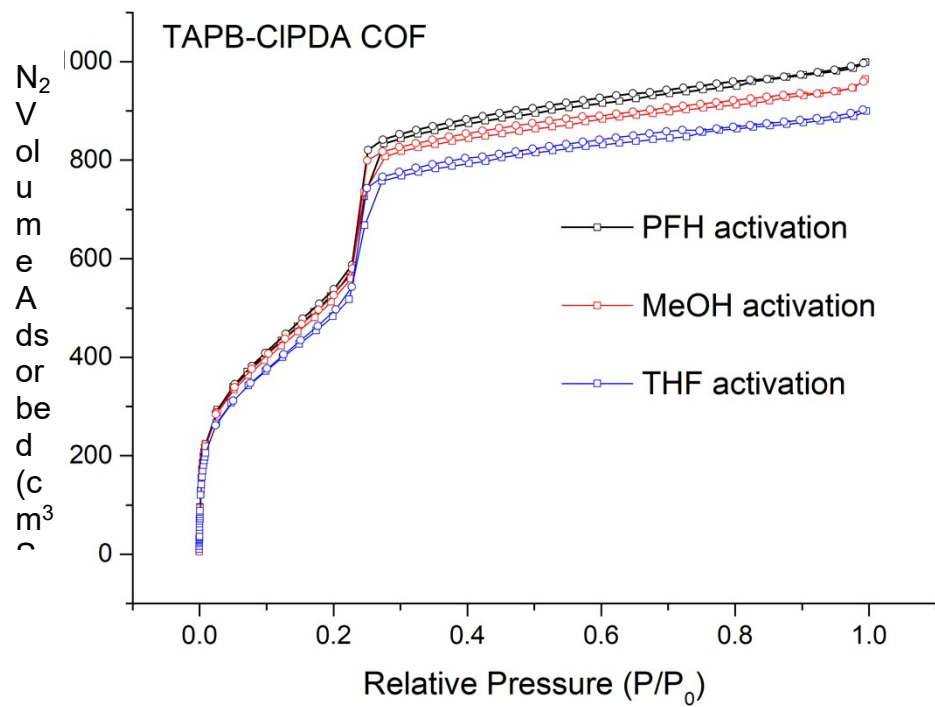


Figure. S21. Nitrogen sorption isotherms for TAPB-CIPDA COFs after activation using PFH, methanol and THF.

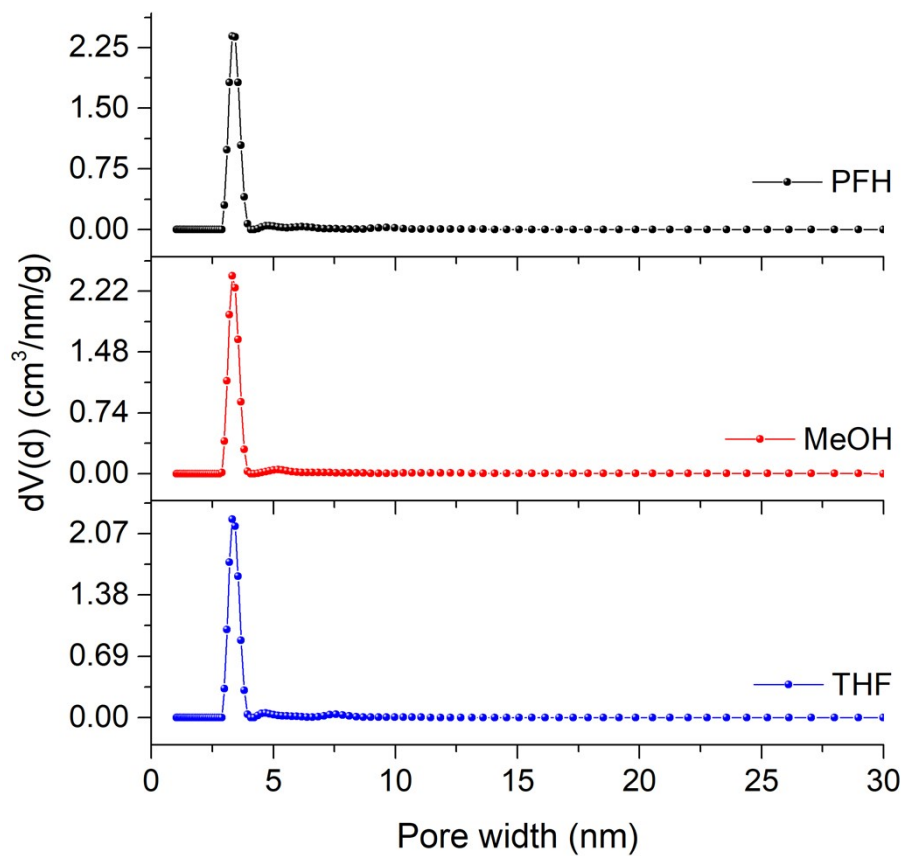


Figure. S22. Pore size distributions of TAPB-CIPDA COF calculated using QSDFT model.

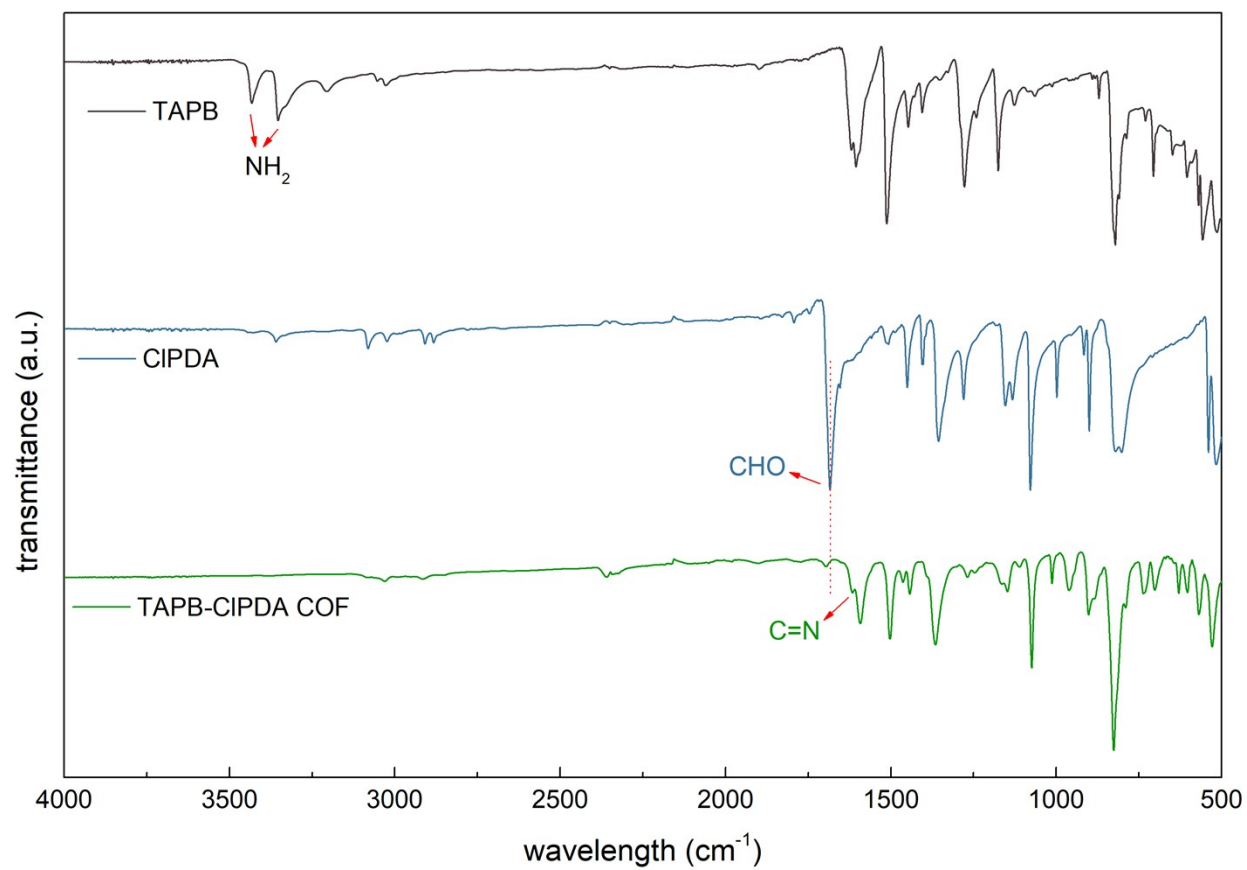


Figure. S23. FTIR spectra of TAPB, CIPDA monomers and TAPB-CIPDA COF.

#### 2.2.4. TAPB-BrPDA COF

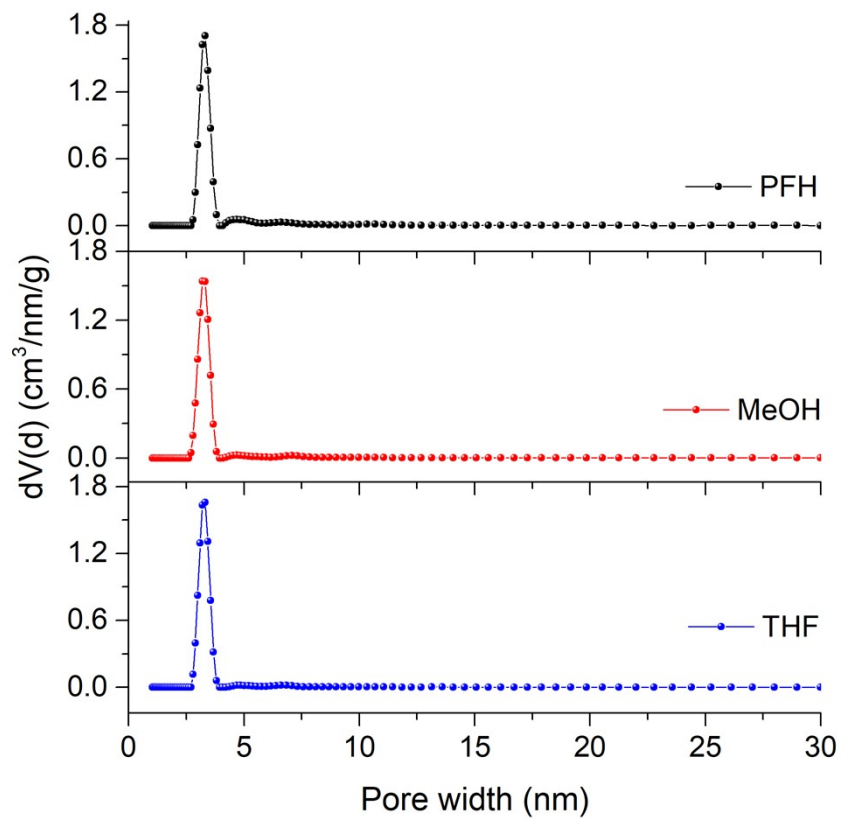


Figure. S24. Pore size distributions of TAPB-BrPDA COFs calculated using QSDFT model.

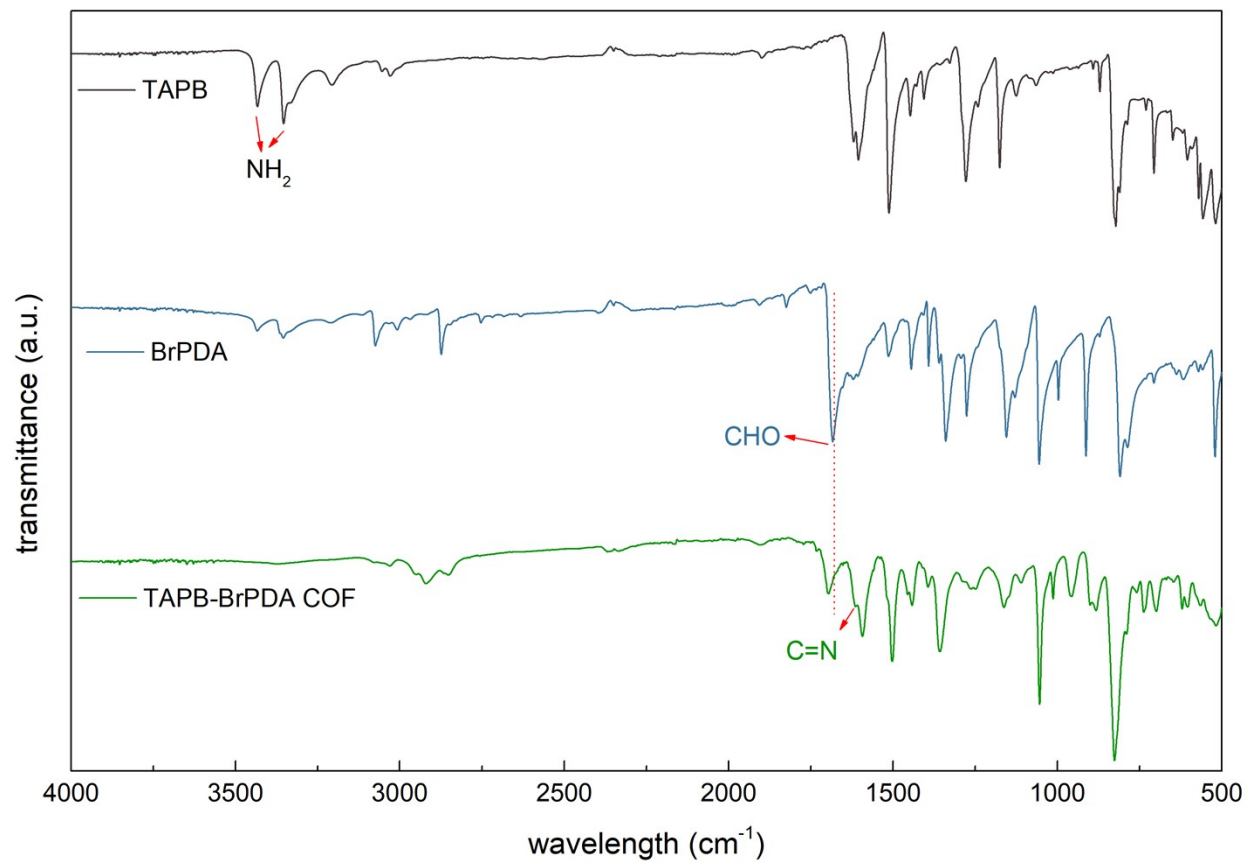


Figure. S25. FTIR spectra of TAPB, BrPDA monomers and TAPB-BrPDA COF.

### 2.2.5. TAPB-OMePDA COF

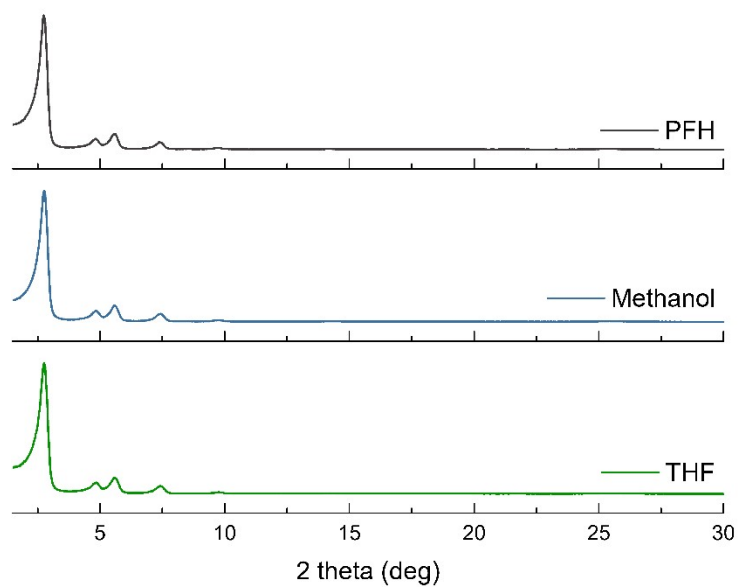


Figure. S26. PXRD patterns from TAPB-OMePDA COFs after activation using PFH, methanol and THF.

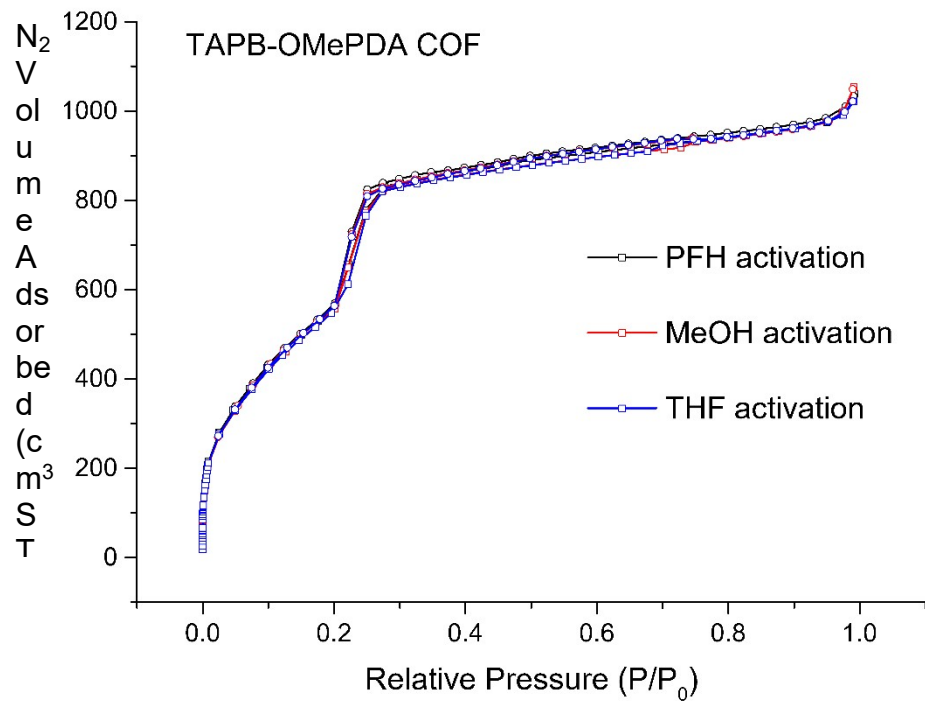


Figure. S27. Nitrogen sorption isotherms after activation using PFH, methanol and THF.

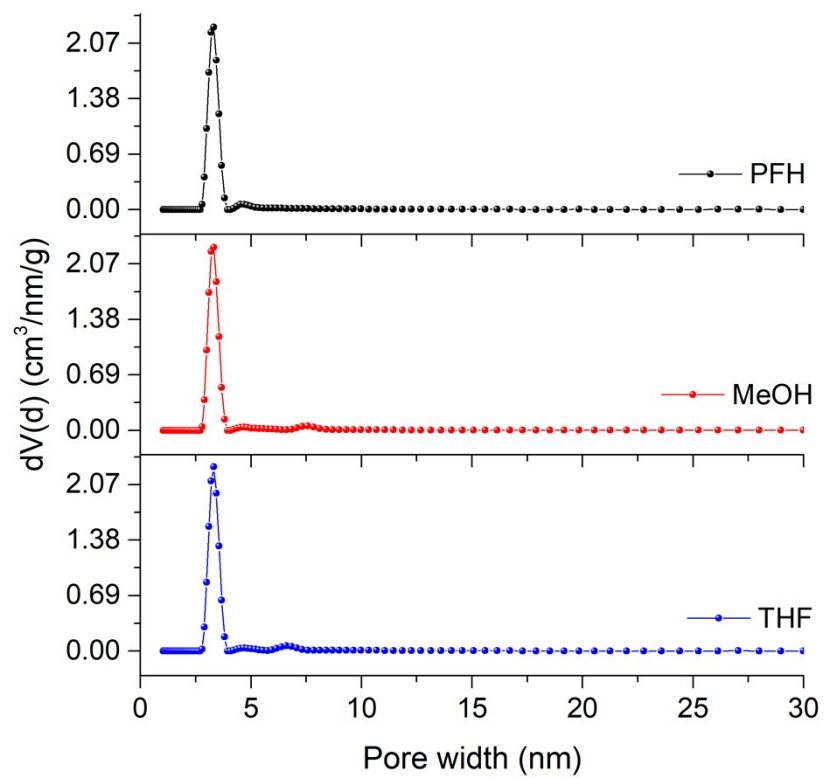


Figure. S28. Pore size distributions of TAPB-OMePDA COF calculated using QSDFT model.

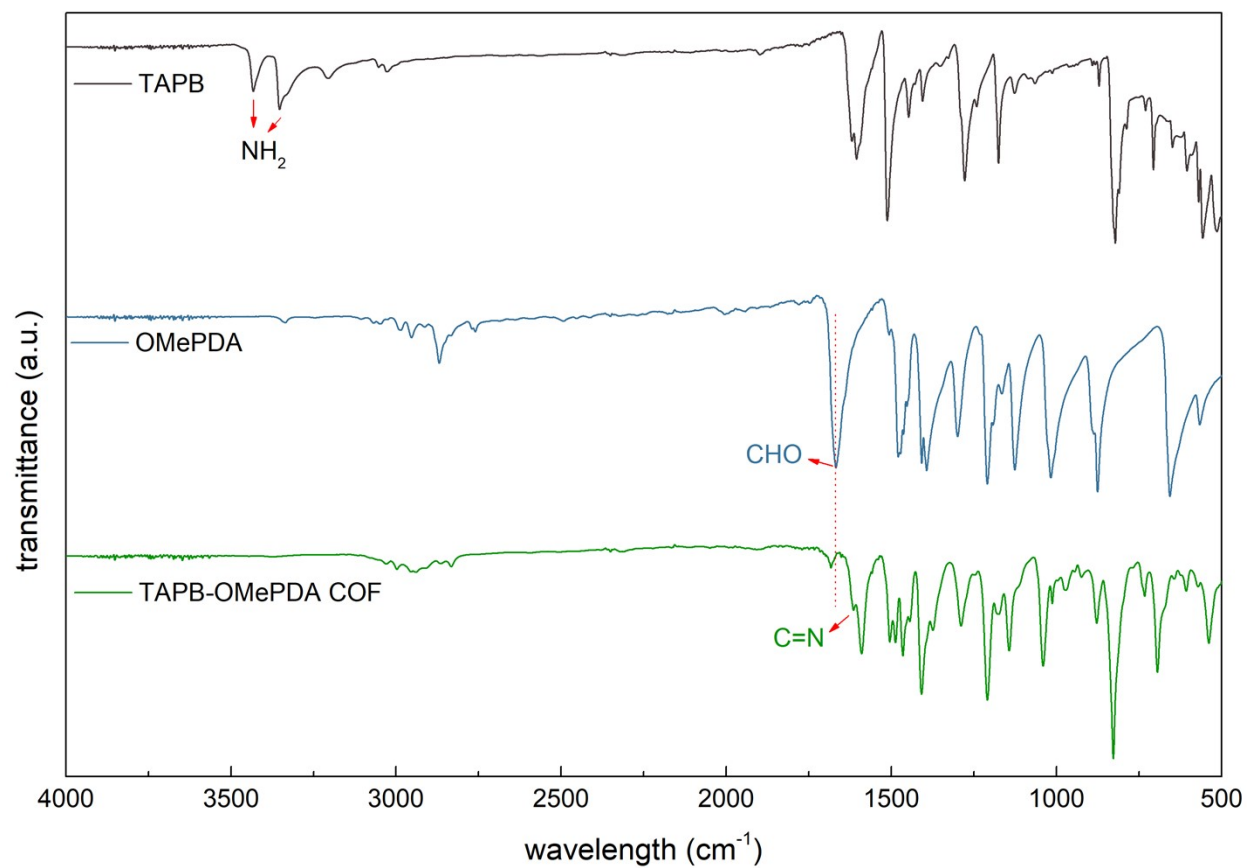


Figure. S29. FTIR spectra of TAPB, OMePDA monomers and TAPB-OMePDA COF.

### 2.2.6. Comparison of fragility for COFs with different pore functionalities

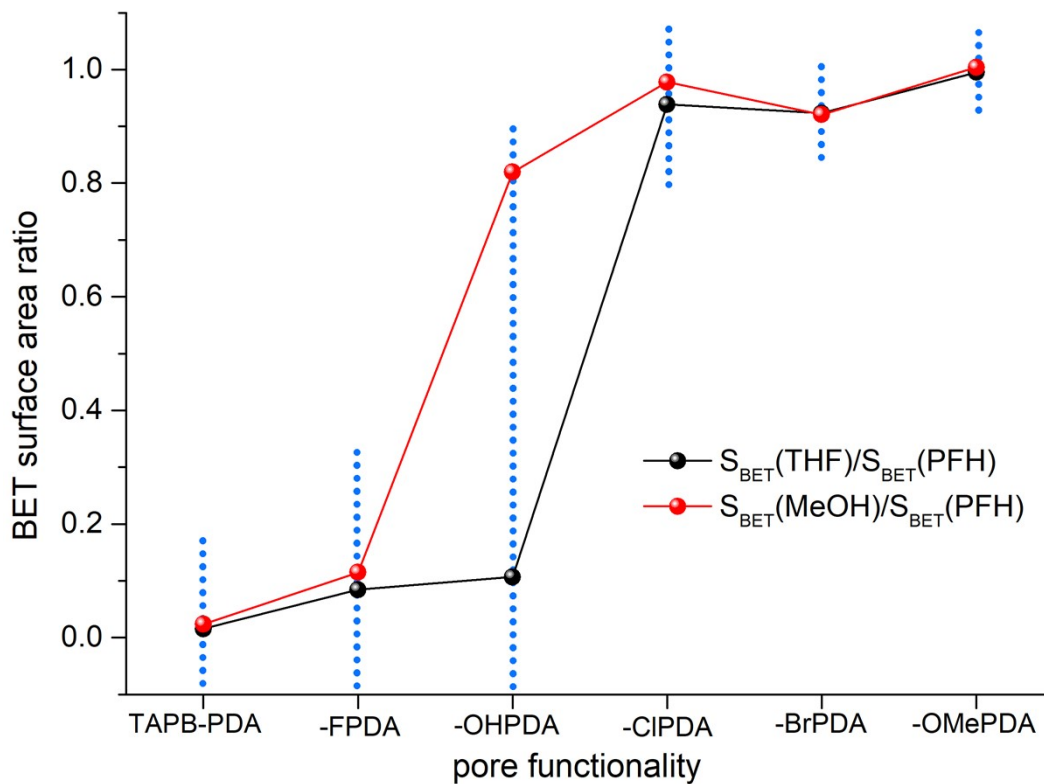


Figure. S30. The ratio of BET surface areas after PFH and THF activation ( $S_{\text{BET}}(\text{THF})/S_{\text{BET}}(\text{PFH})$ ) and those after MeOH and THF activation ( $S_{\text{BET}}(\text{THF})/S_{\text{BET}}(\text{MeOH})$ ). The substituents are ordered in terms of their impact on activation stability, not in terms of size or polarity.

## 2.3. Pore architecture series

### 2.3.1. Py-1P COF

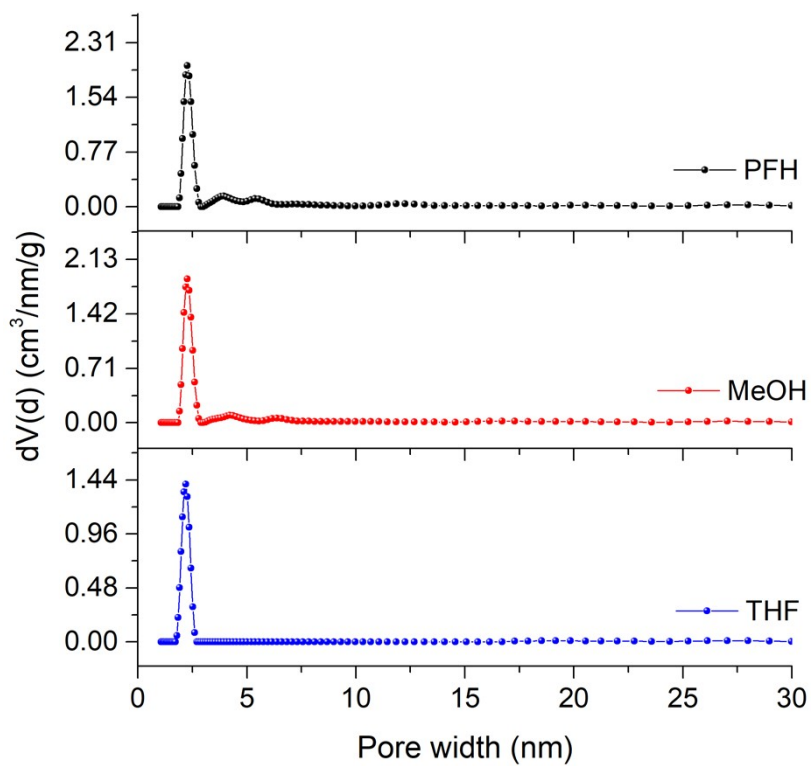


Figure. S31. Pore size distributions of Py-1P COF calculated using QSDFT model.

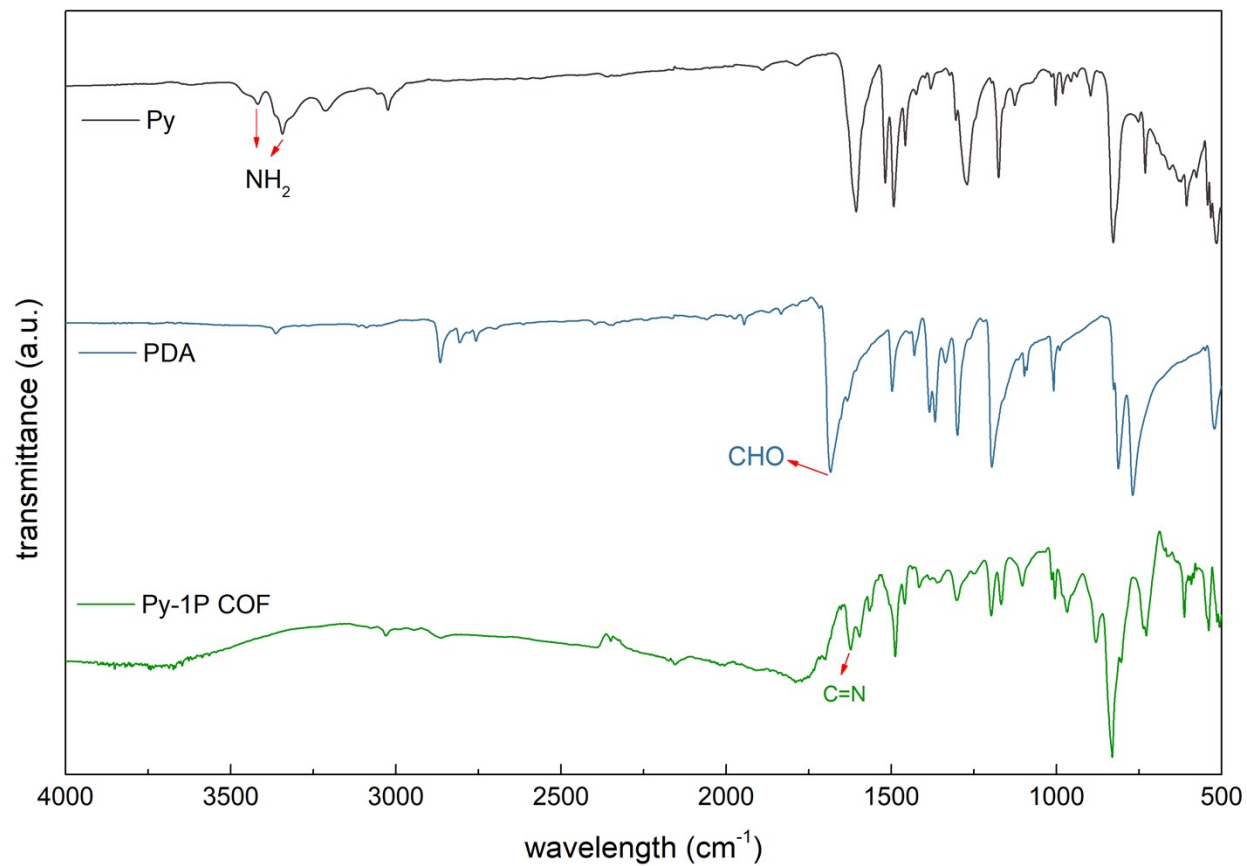


Figure. S32. FTIR spectra of Py, PDA monomers and Py-1P COF.

### 2.3.2. Py-2P COF

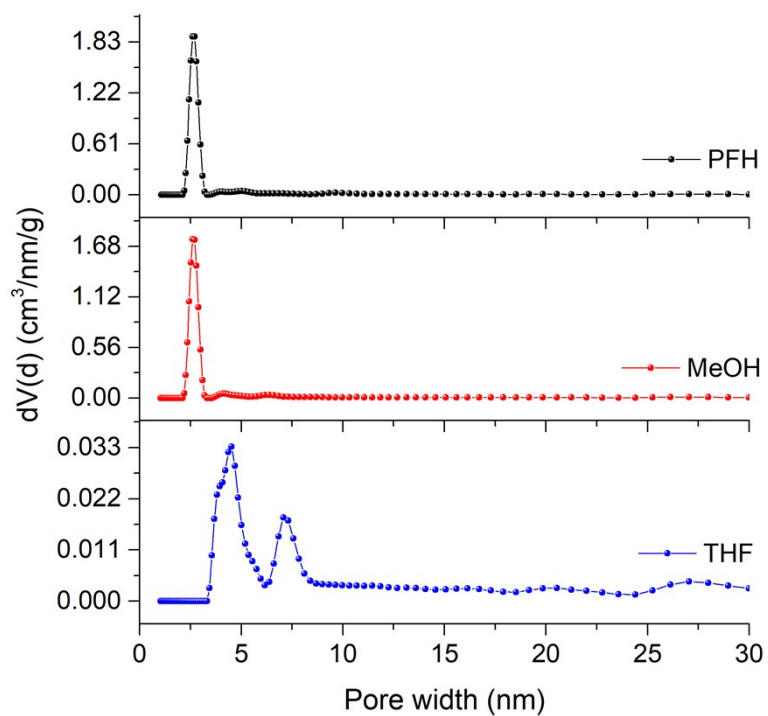


Figure. S33. Pore size distributions of Py-2P COF calculated using QSDFT model.

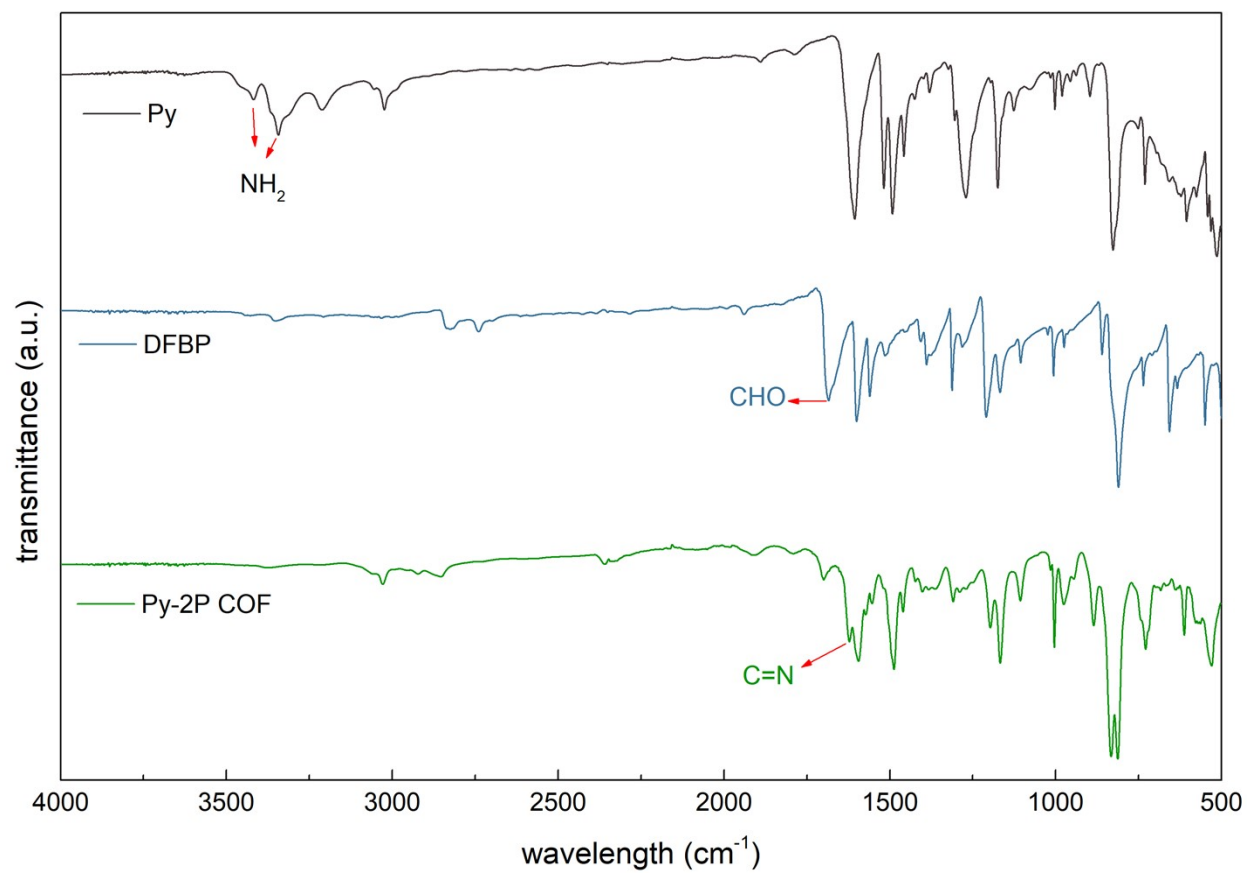


Figure. S34. FTIR spectra of Py, DFBP monomers and Py-2P COF.

### 2.3.3. Py-OH1P COF

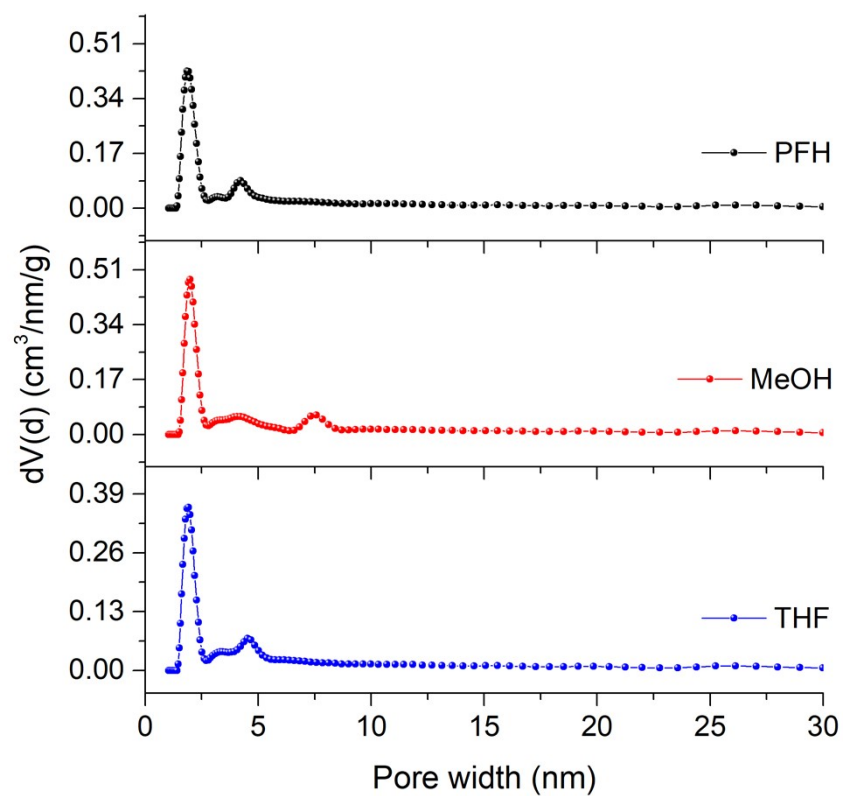


Figure. S35. Pore size distributions of Py-OH1P COF calculated using QSDFT model.

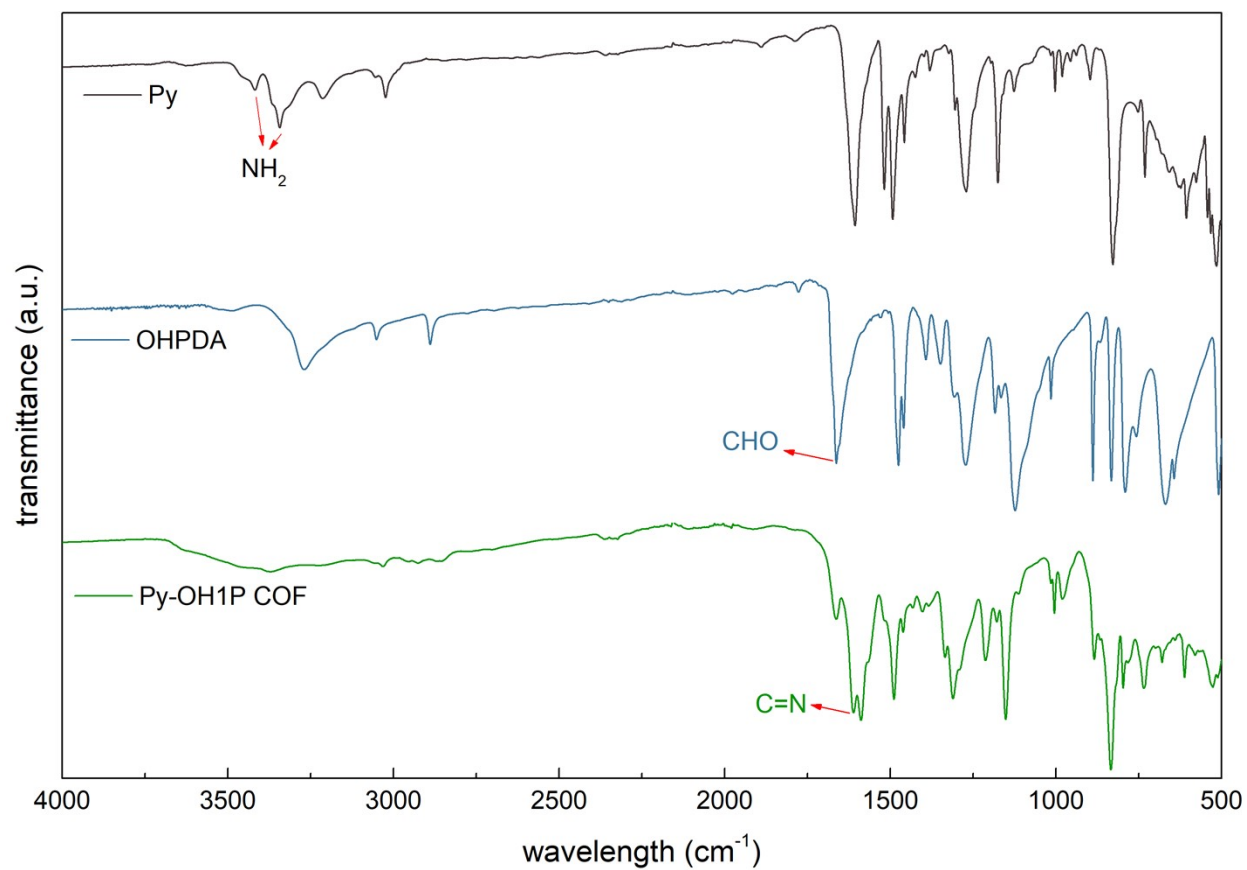


Figure. S36. FTIR spectra of Py, OHPDA monomers and Py-OH1P COF.

### 2.3.4. Py-OMe3P COF

Py-OMe3P COF has not been reported, so we did the Pawley refinement and simulated its structure. Structural modeling of COFs was generated using the Materials Studio program employing the Building (Crystal) module, The lattice model was geometrically optimized using force-filed based method (Forcite, UFF, Qeq, Ewald summations) and SCC-DFTB (DFTB + module). The Pawley fitting (Reflex module) was performed to optimize the lattice parameters iteratively until the Rwp value converges and the overlay of the observed with refined profiles shows good agreement. We have deposited the crystallographic information file of the Py-OMe3P COF to the CCDC database with a deposition number: 2191120.

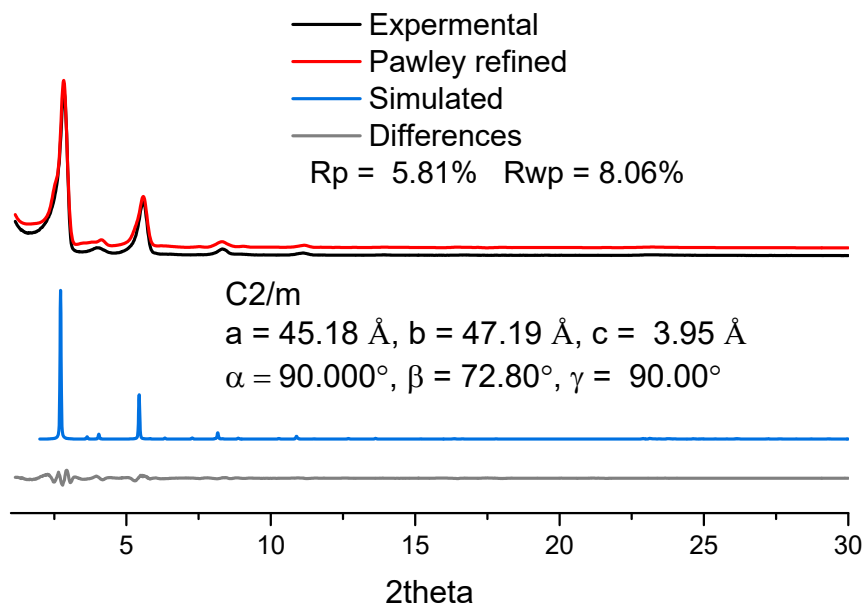


Figure. S37. Experimental, Pawley refined and simulated PXRD for Py-OMe3P COF.

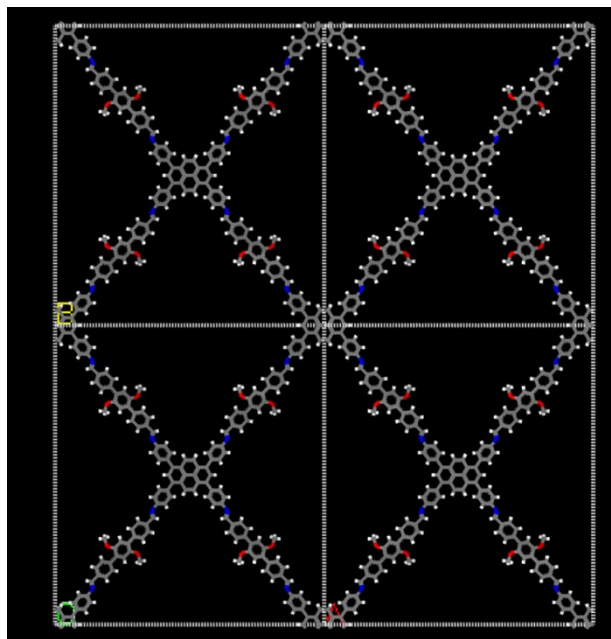


Figure. S38. Simulated structure for Py-OMe3P COF.

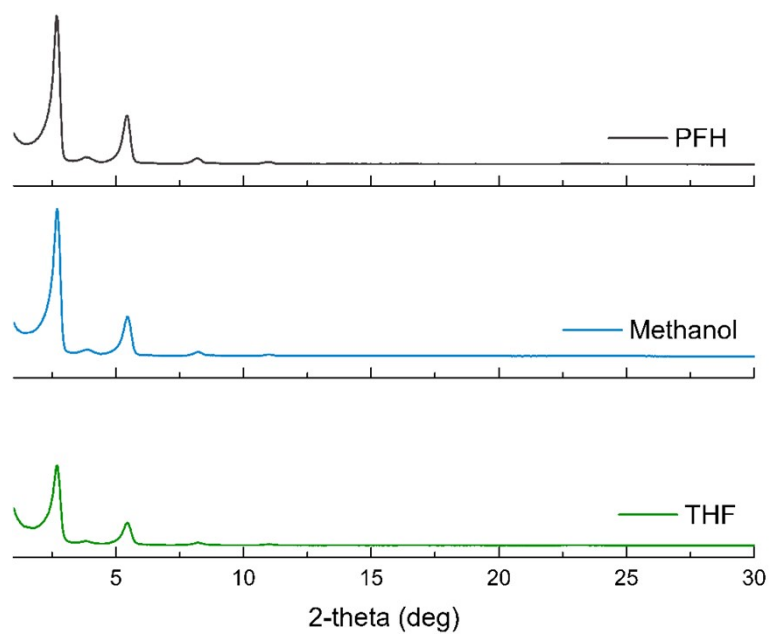


Figure. S39. PXRD spectra of Py-OMe3P COFs activated using PFH, methanol and THF.

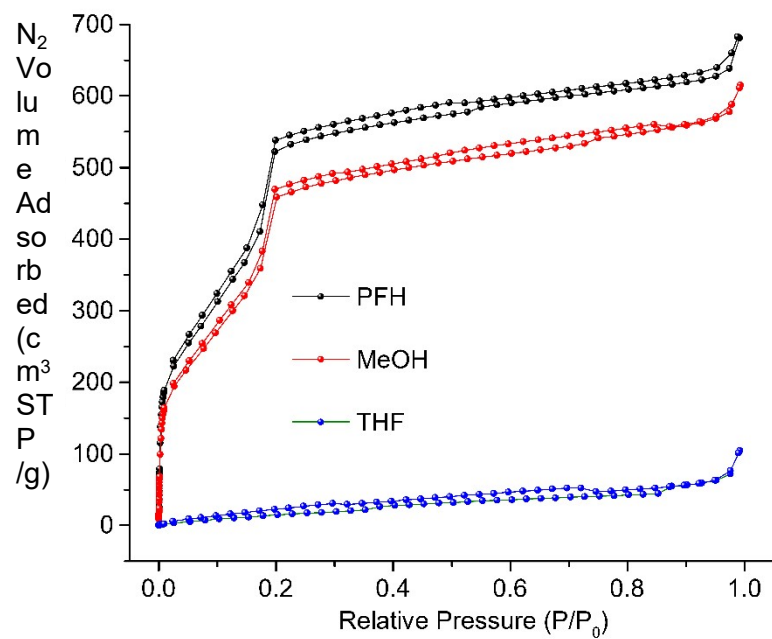


Figure. S40. Nitrogen isotherms for Py-OMe3P COFs activated using PFH, methanol and THF.

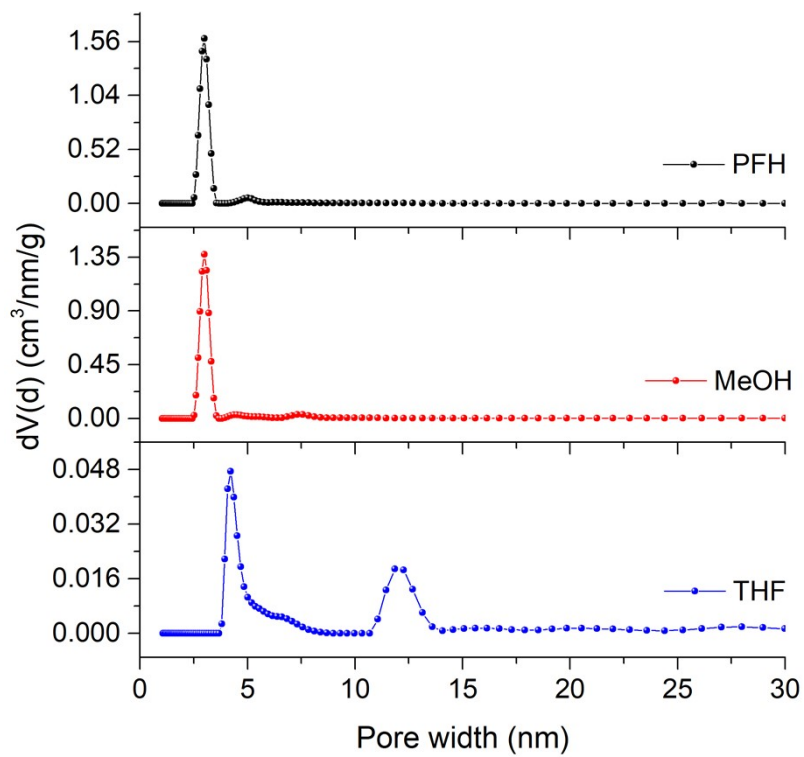


Figure. S41. Pore size distributions of Py-OMe3P COF calculated using QSDFT model.

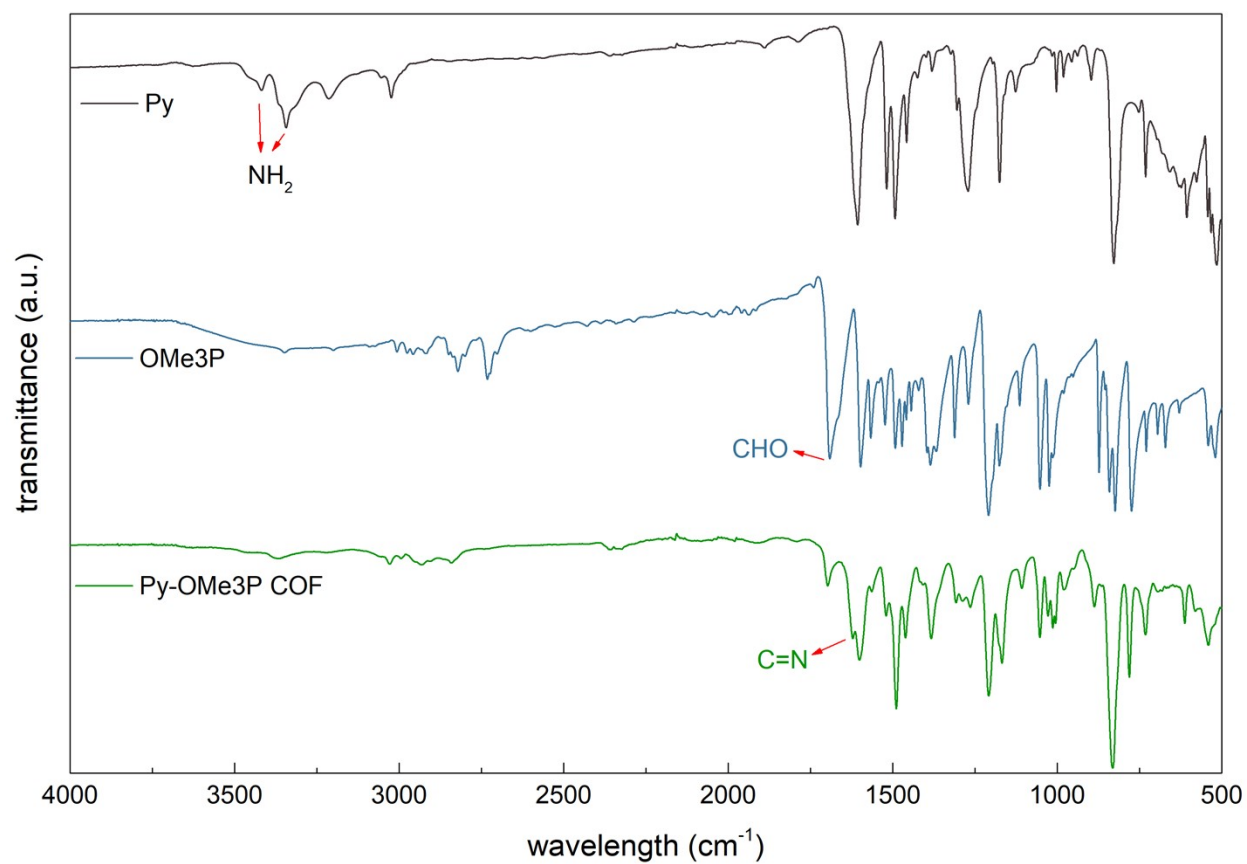


Figure. S42. FTIR spectra of Py, OMe3P monomers and Py-OMe3P COF.

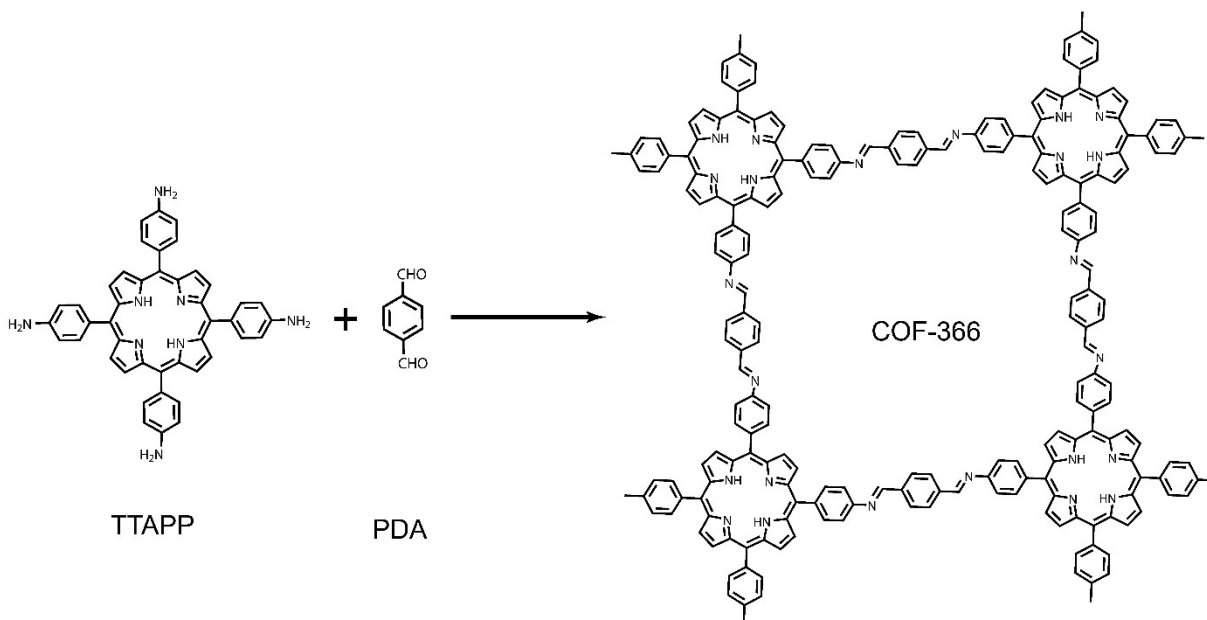
### 2.3.5. Porphyrin COFs

In addition to hexagonal and rhombic topology, COFs with tetragonal topology are also widely investigated and represent the typical COF types with homogenous pore structures. We designed a series of COFs with tetragonal topology using the porphyrin nodes and different aldehyde linkers including linkers with different length and functionalities. However, possibly due to the low solubility of 5,10,15,20-tetrakis(4-aminophenyl)porphyrin (TTAPP), highly crystalline and porous COFs with tetragonal topology could not be produced even after PFH activation. Therefore, it is difficult to compare the solvent activation effect on these samples. The synthesis trials and characterization results are shown below.

Synthesis of porphyrin-based COFs (COF-366, COF-367, COF-366-OMe). The synthesis conditions for porphyrin-based COFs follow a prior publication.<sup>6,7</sup> The detailed synthesis of COF-366 is described here. 0.04 mmol 5,10,15,20-tetrakis(4-aminophenyl)porphyrin (TTAPP) and 0.08 mmol terephthalaldehyde (PDA) were weighed and placed in a Pyrex tube, then a solvent mixture of 0.34 mL benzyl alcohol and 0.66 mL mesitylene was added. To uniformly disperse the monomers, the Pyrex tube was sonicated for 5 minutes and followed by addition of 0.1 mL 6M acetic acid as the catalyst. Finally, the Pyrex tube was flame sealed and placed in oven to react at 120 °C for 5 days. To separate the dry COF-366 powders, the produced precipitates were thoroughly washed using THF and acetone thorough centrifugation. In the last washing step, perfluorohexane was used to avoid pore collapse. After vacuum dried at 80 °C under vacuum overnight, the samples were measured for PXRD, BET and FTIR analysis. However, all COF-366, COF-367 and COF-366-OMe showed limited crystallinity and limited porosity, which are not appropriate to be used as cases for pore collapse analysis. To note, we also tried to use solvent

system composed of ethanol and mesitylene as reported by Yaghi and coworker,<sup>7</sup> and solvent mixture of dioxane/mesitylene or o-dichlorobenzene/1-butanol, but none of them could produce crystalline porphyrin-based COFs.

## 1. COF-366



Scheme S1. Scheme for synthesis of COF-366.

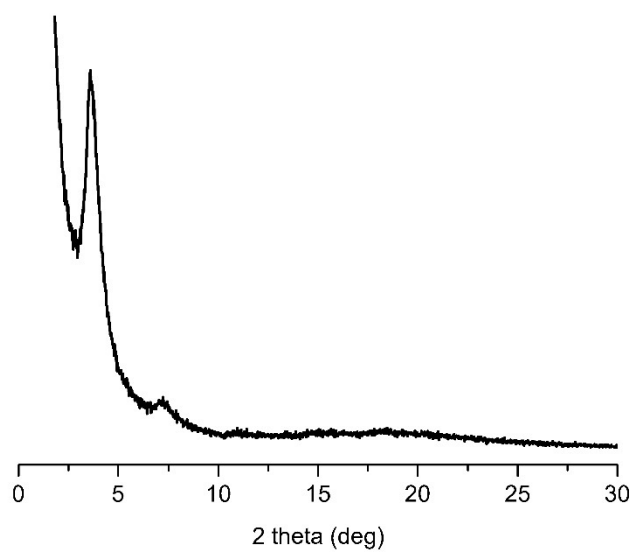


Figure. S43. PXRD pattern for COF-366 after PFH activation.

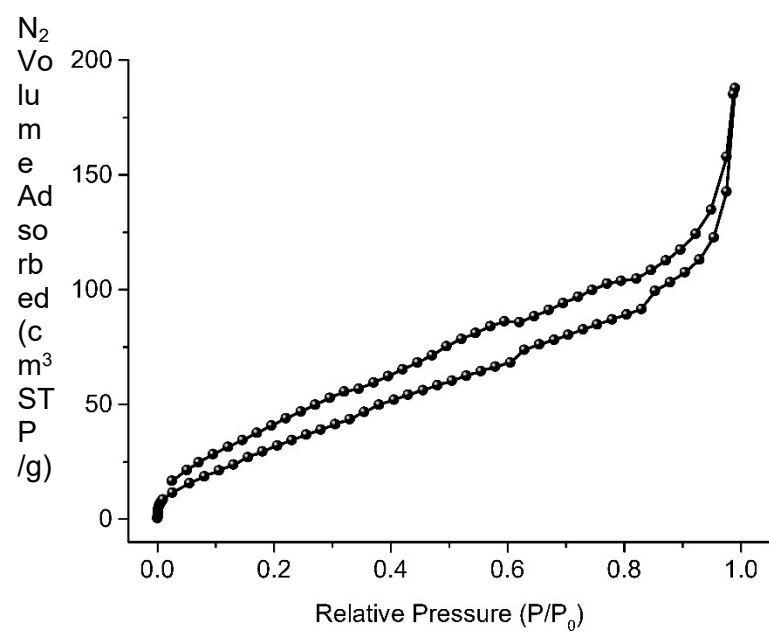


Figure. S44. Nitrogen sorption isotherms for COF-366 after PFH activation.

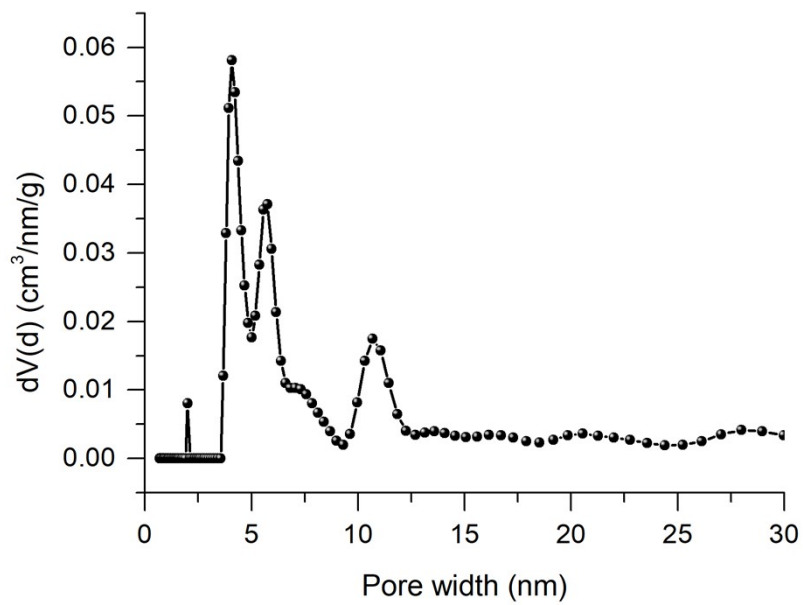


Figure. S45. Pore size distributions of COF-366 calculated using QSDFT model.

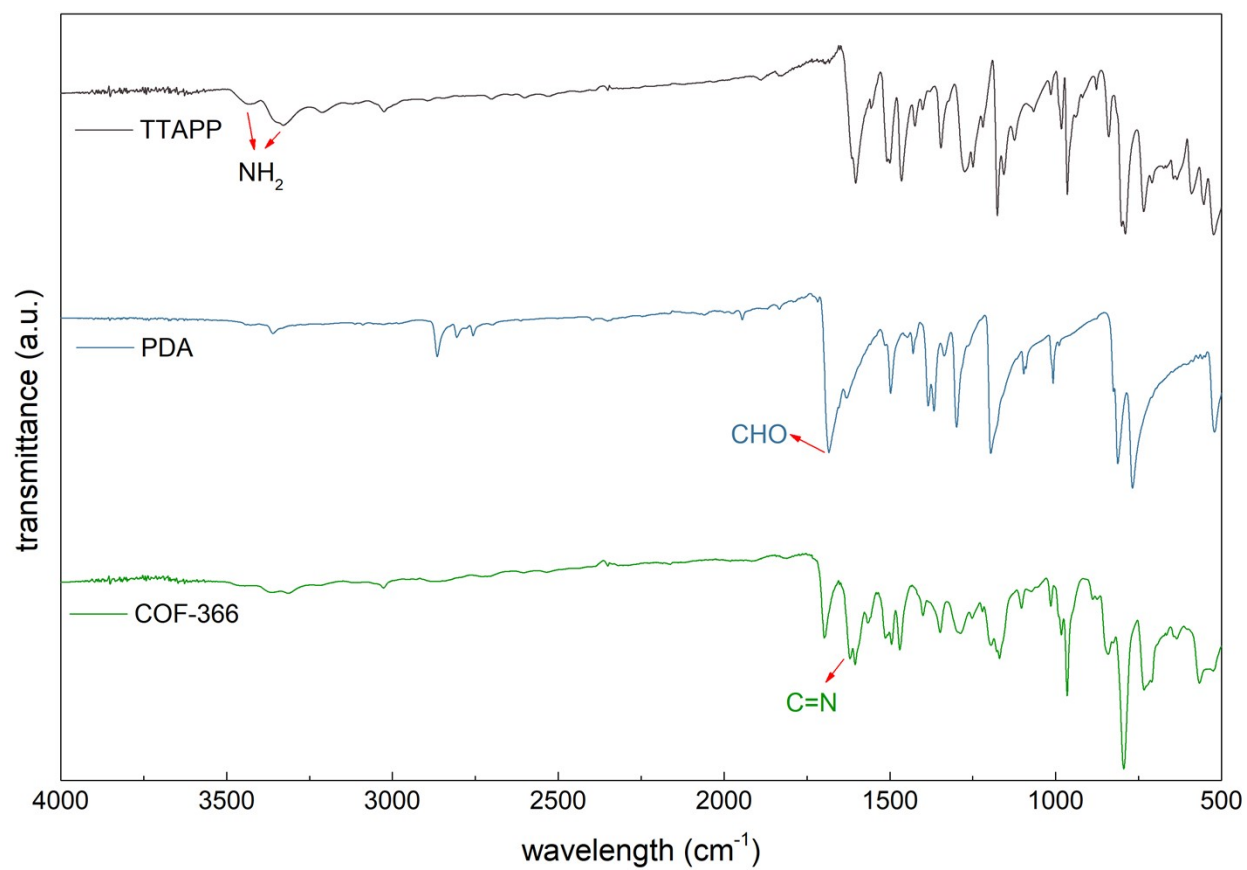
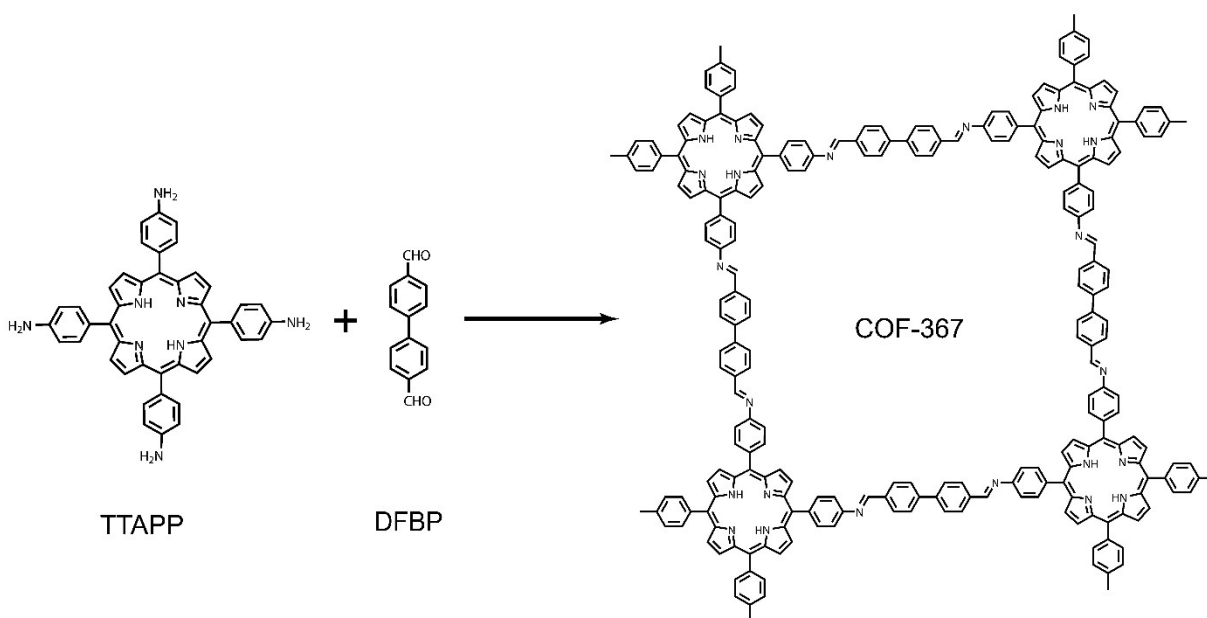


Figure. S46. FTIR spectra for TTAPP, PDA and COF-366.

## 2. COF-367



Scheme S2. Scheme for the synthesis of COF-367.

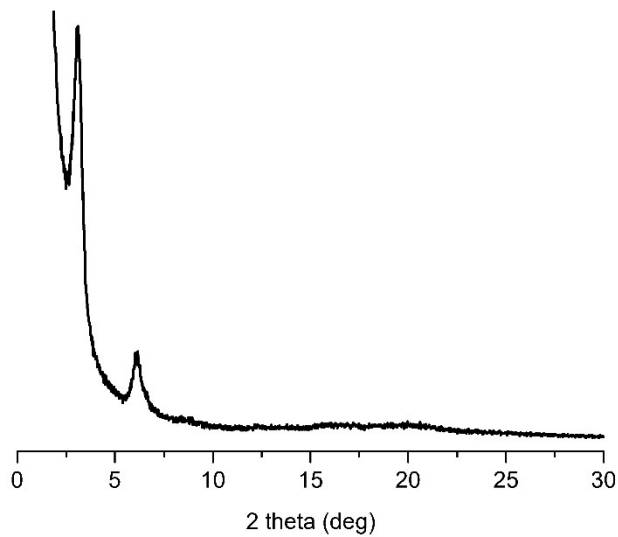


Figure. S47. PXRD pattern for COF-367 after PFH activation.

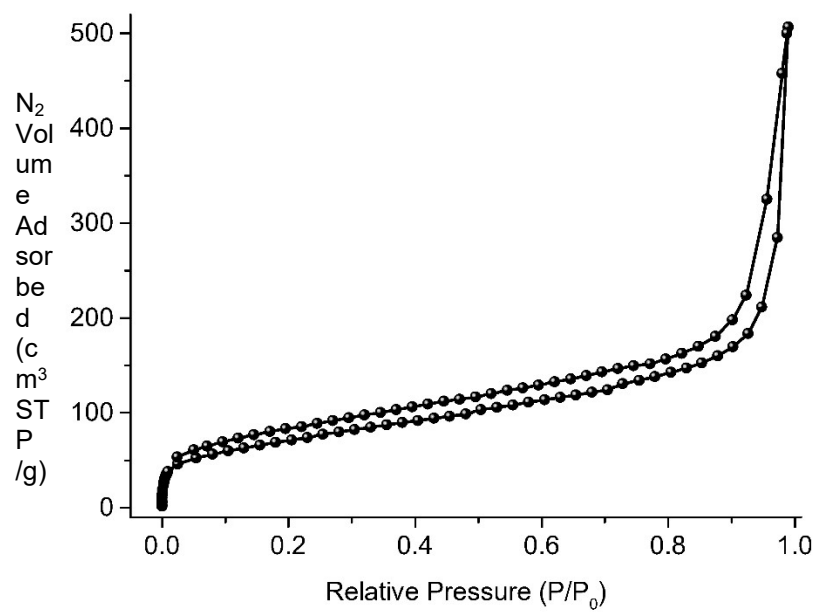


Figure. S48. Nitrogen sorption isotherms for COF-367.

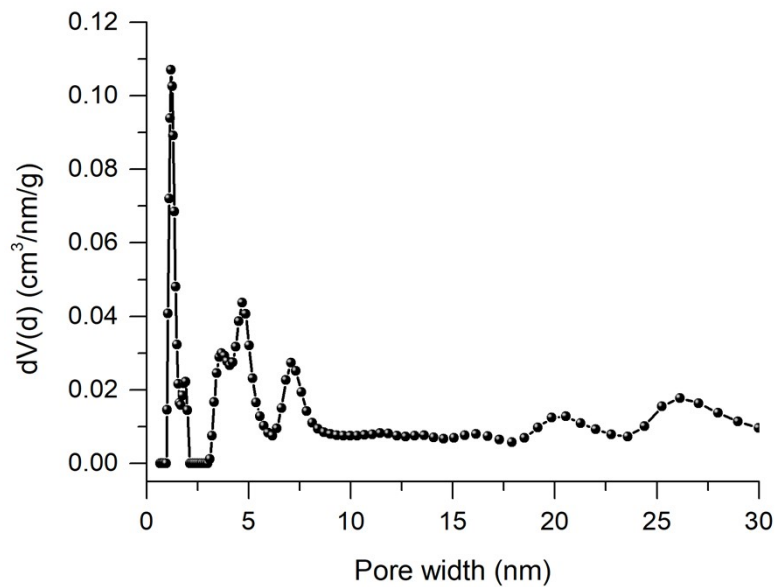


Figure. S49. Pore size distributions of COF-367 calculated using QSDFT model.

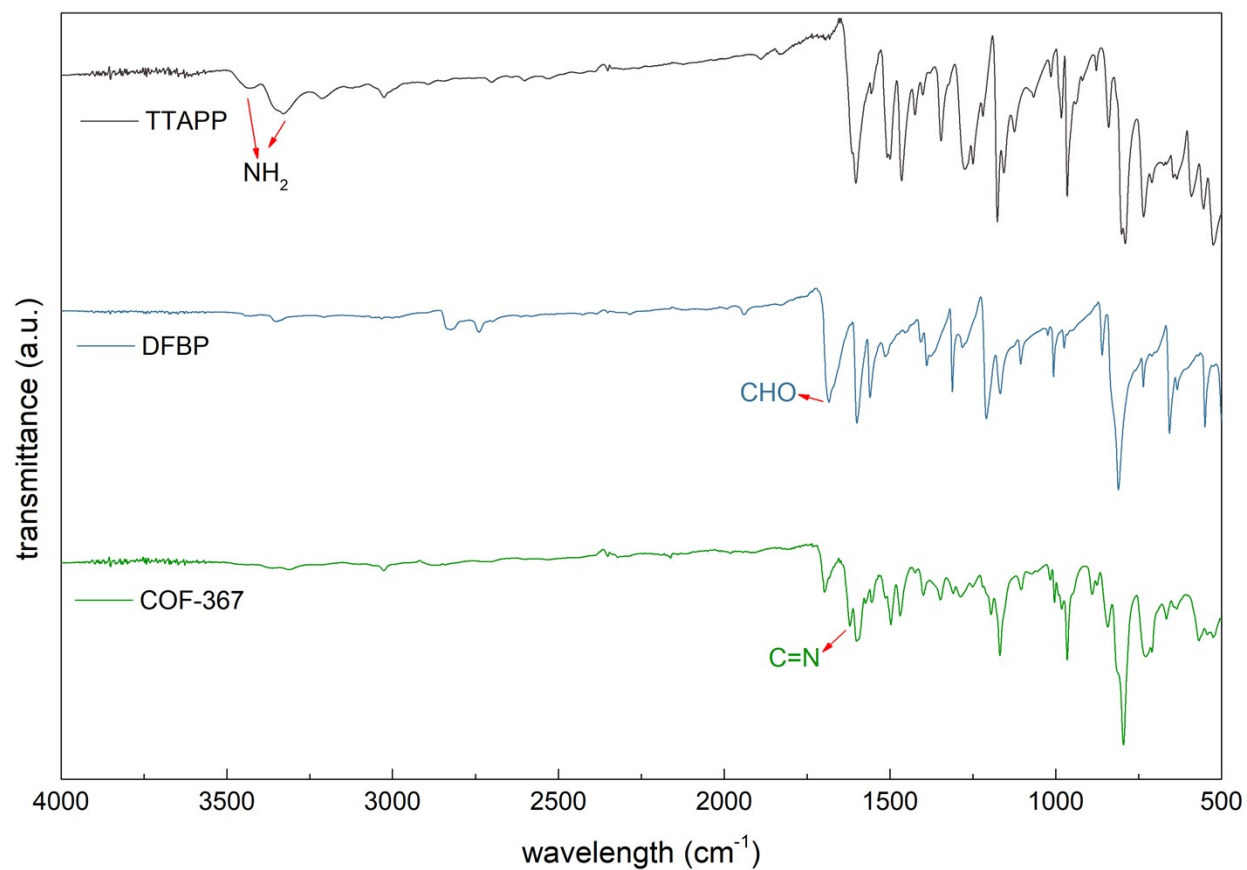
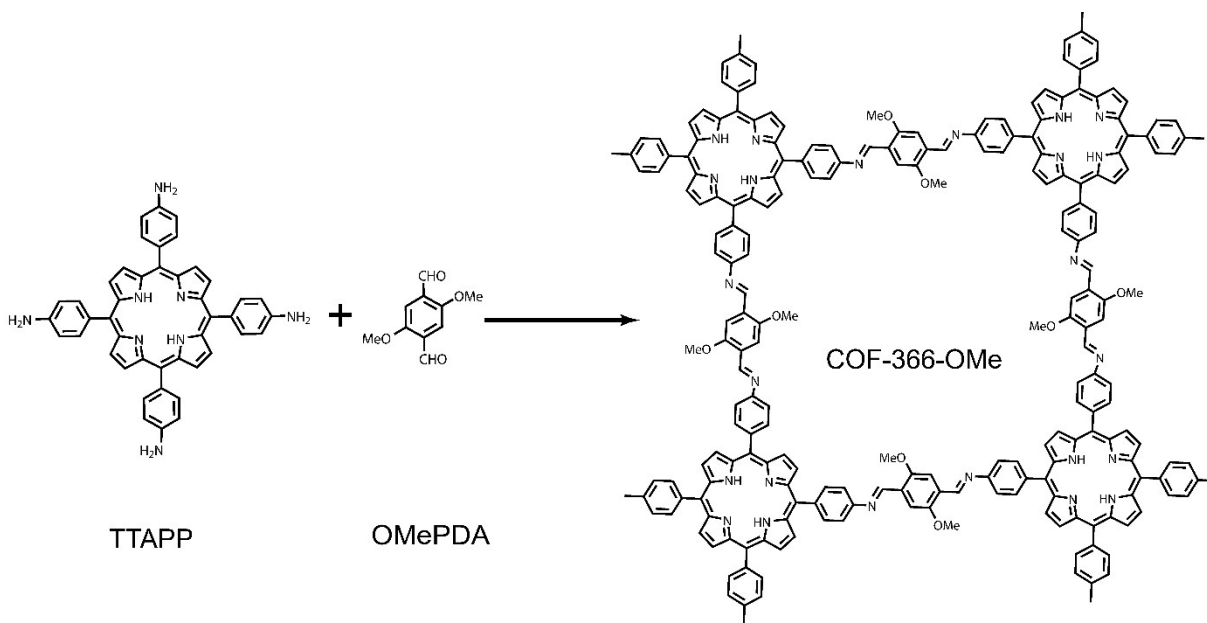


Figure. S50. FTIR spectra for TTAPP, DFBP and COF-367.

### 3. COF-366-OMe



Scheme S3. Scheme for the synthesis of COF-366-OMe.

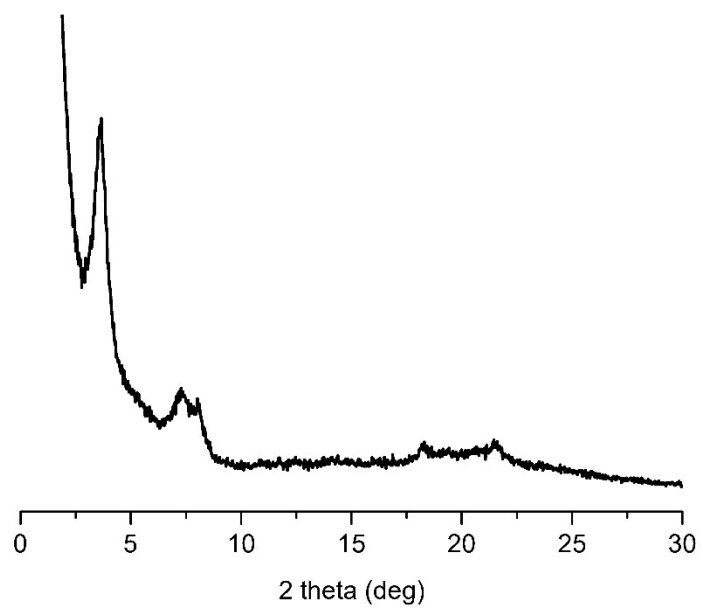


Figure. S51. PXRD for COF-366-OMe after PFH activation.

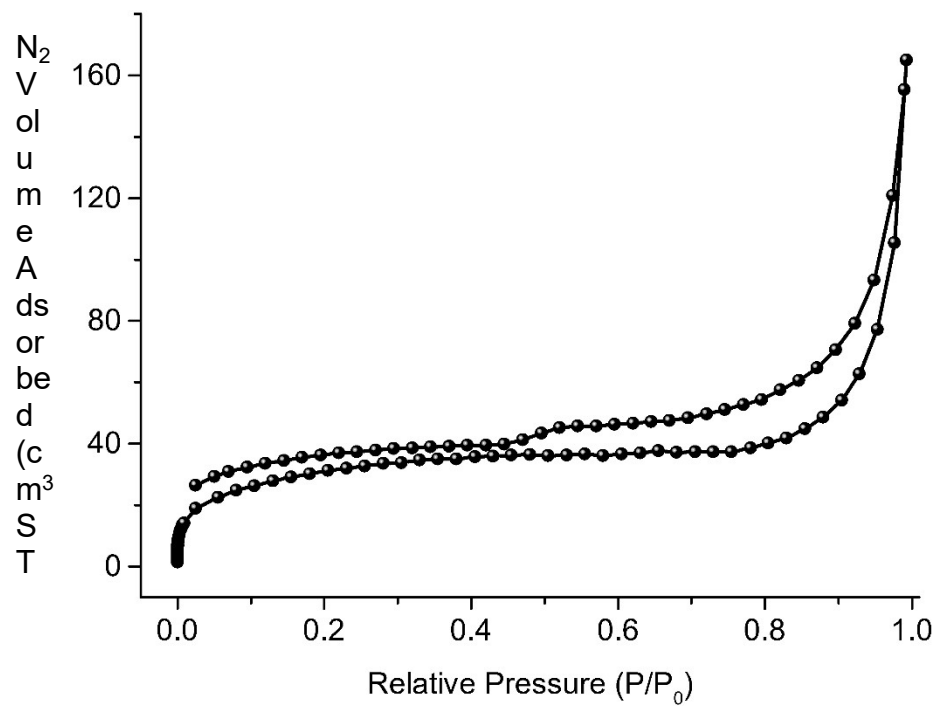


Figure. S52. Nitrogen sorption isotherms for COF-366-OMe.

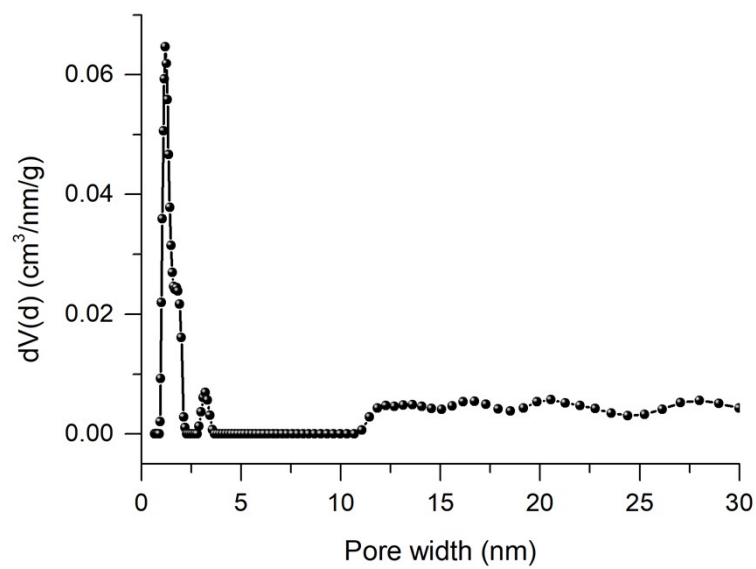


Figure. S53. Pore size distributions of COF-366-OMe calculated using QSDFT model.

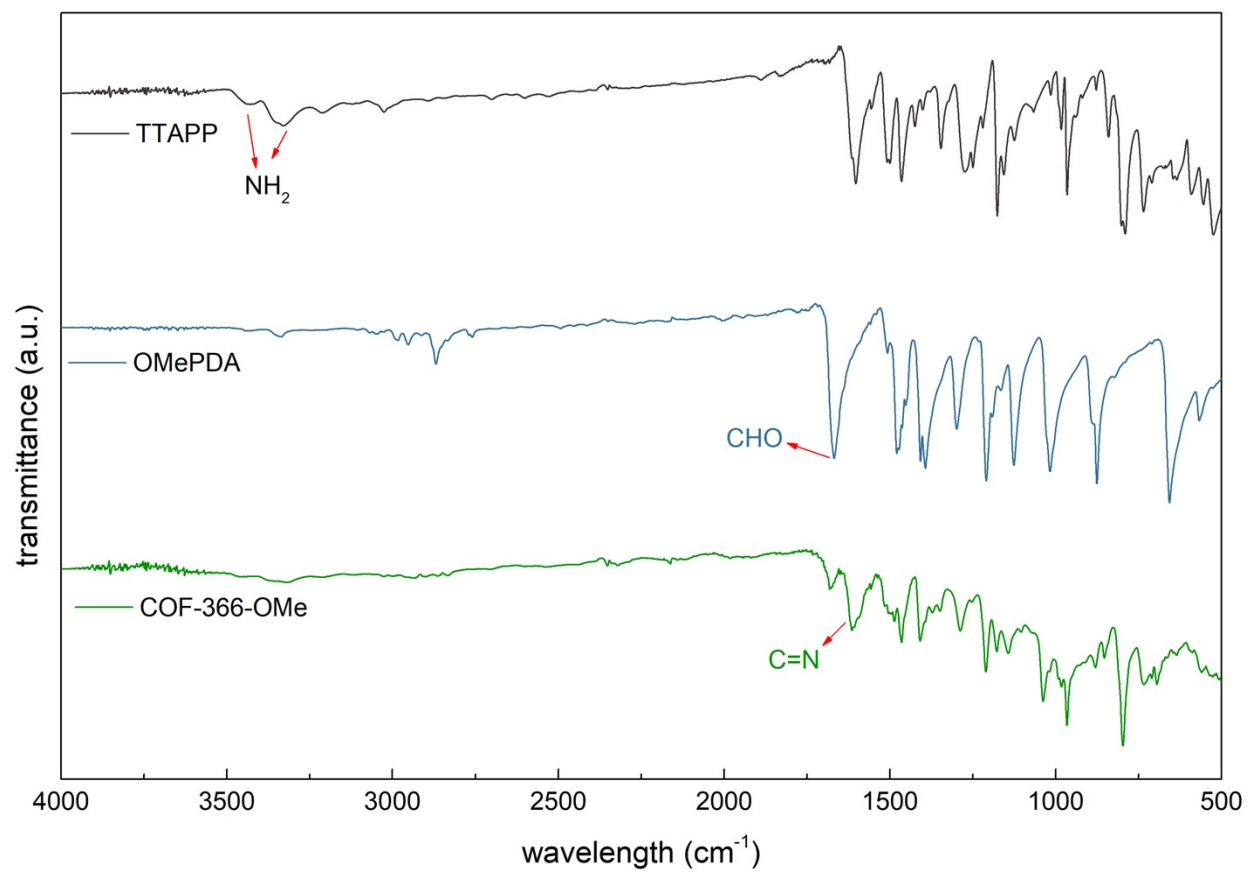


Figure. S54. FTIR spectra for TTAPP, OMePDA and COF-366-OMe.

## 2.4. DFT calculation

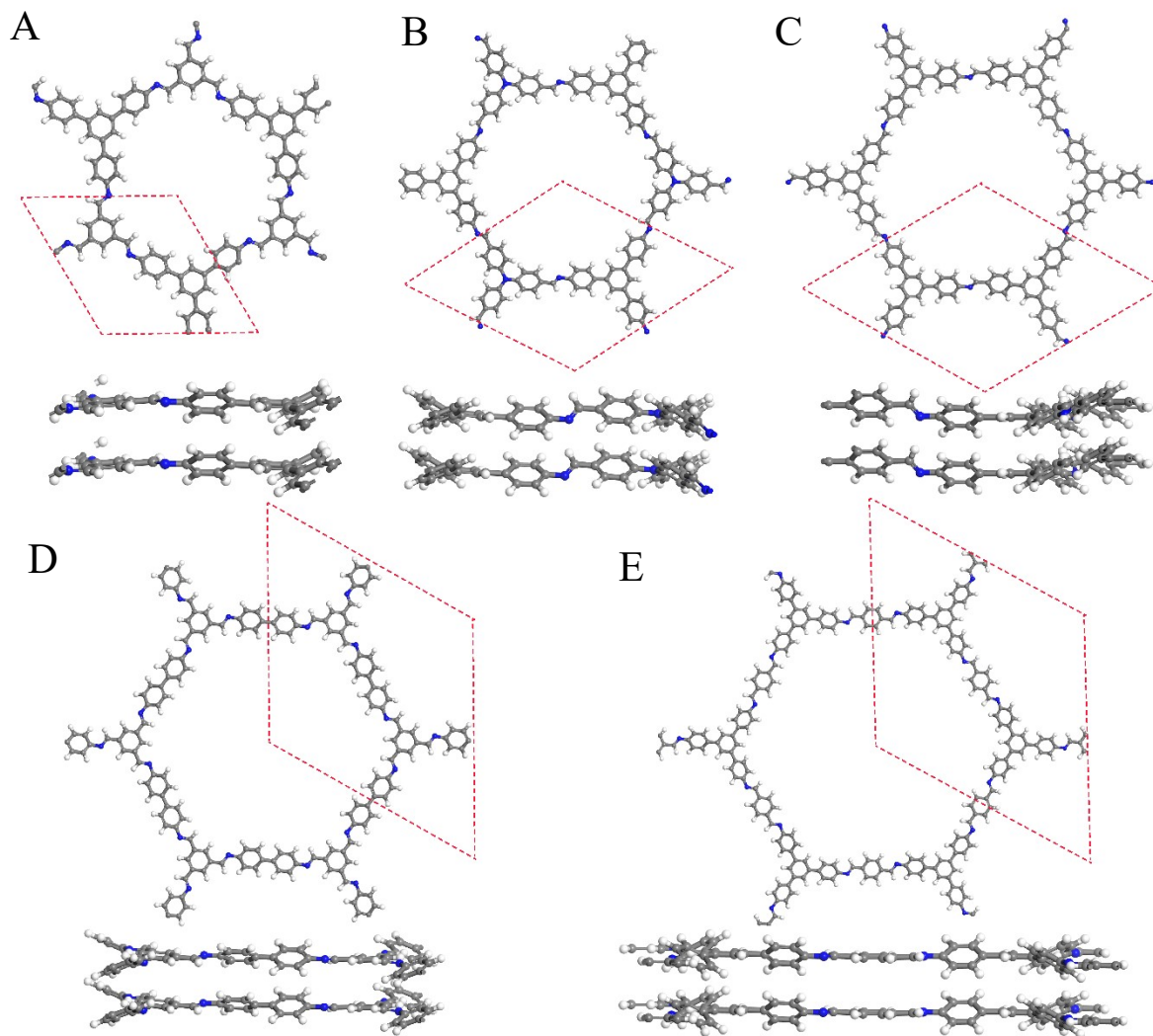


Figure. S55. Crystal models for different COFs with different pore sizes. (a) TAPB-BTCA COF (b) TAPB-TFPA COF (c) TAPB-TFPB COF (d) PI-2 COF (e) TAPB-PDA COF

The crystal model was performed using the plane wave basis Vienna ab initio simulation package (VASP) code. [1-2] The generalized gradient approximation in the Perdew-Burke-Ernzerhof (GGA-PBE) formulation are used with a cutoff energy of 600 eV. The vacuum space of  $\sim 20$  Å is intercalated into interlamination to eliminate the interaction between layers. A  $6 \times 6$  2D

grid uniform k-points is applied for Density-functional theoretical (DFT) calculations. The van der Waals (vdW) corrections were employed (DFT-D3) to calculate the interlayer distance in bulk phases.

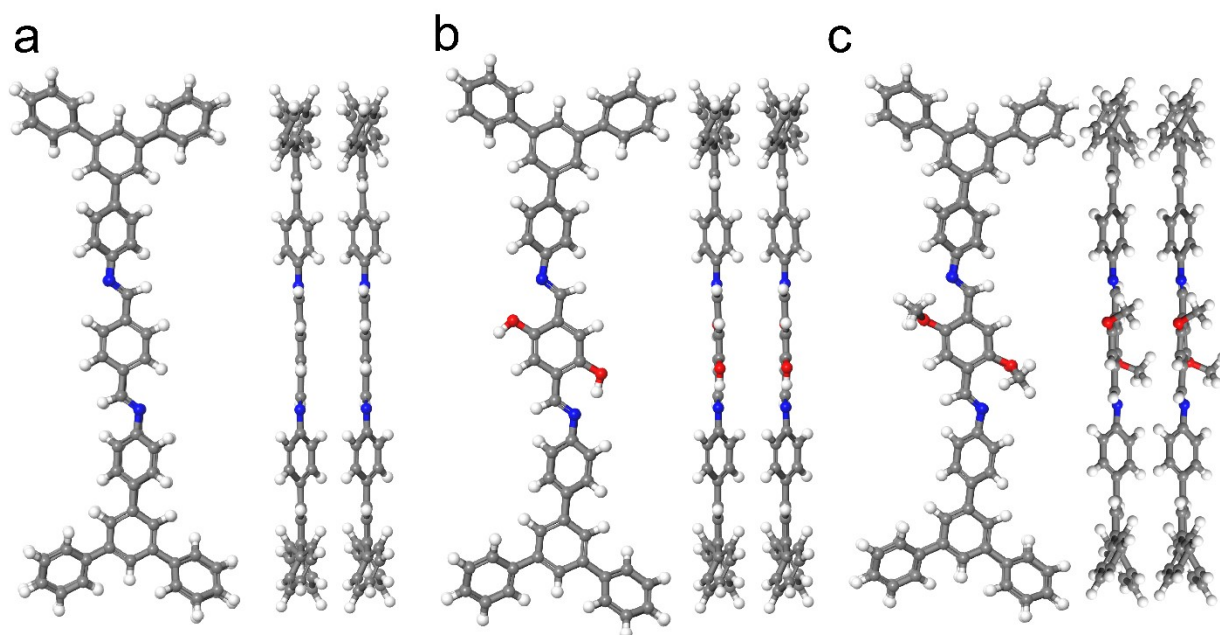


Figure. S56. Molecular models for the COFs studied with different side functionalities (a) molecular model for TAPB-PDA COF (b) molecular model for TAPB-OHPDA COF (c) molecular model for TAPB-OMePD COF.

To focus on the local interlayer interactions caused by side functionalities, we simplified the COF models by using molecular models and reduced the calculation working load. The molecular model was carried out with the Gaussian 16 code based on DFT. [3] The Becke exchange functional (B) and the Lee–Yang–Parr (LYP) correlation functional within a generalized gradient approximation (GGA) was used to describe the interaction between the ionic cores and electrons. [4-5] The hybrid basic set b3lyp/6-311+g(d,p) was employed to optimize all structures and calculate total energy.

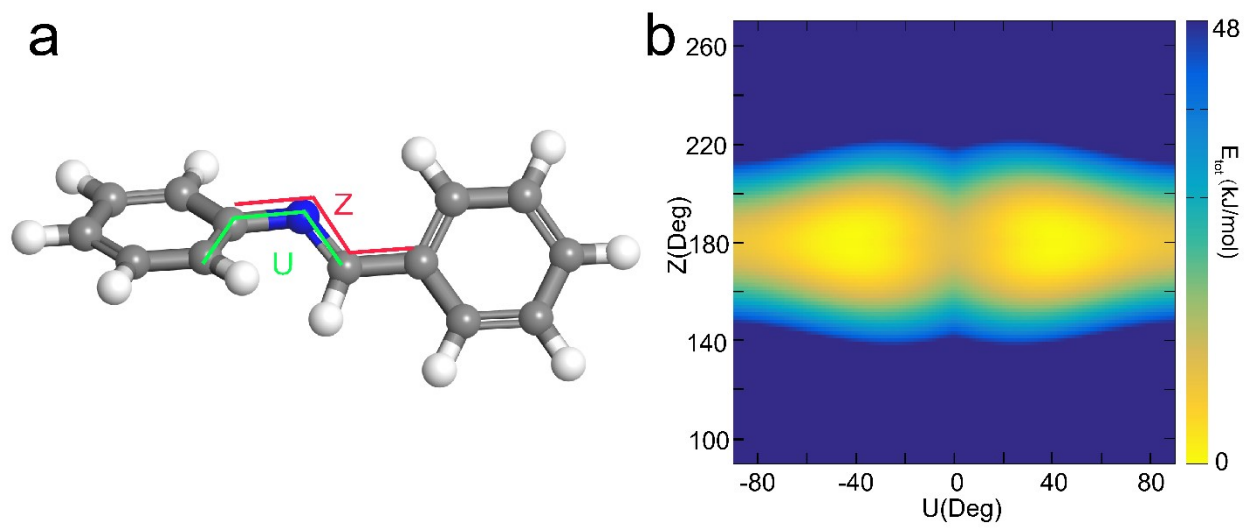


Figure. S57. (a) Two types of dihedral angles U and Z between two benzenes along the C=N linkage. (b) Calculated energy surface as functions of U and Z for the model in (a).

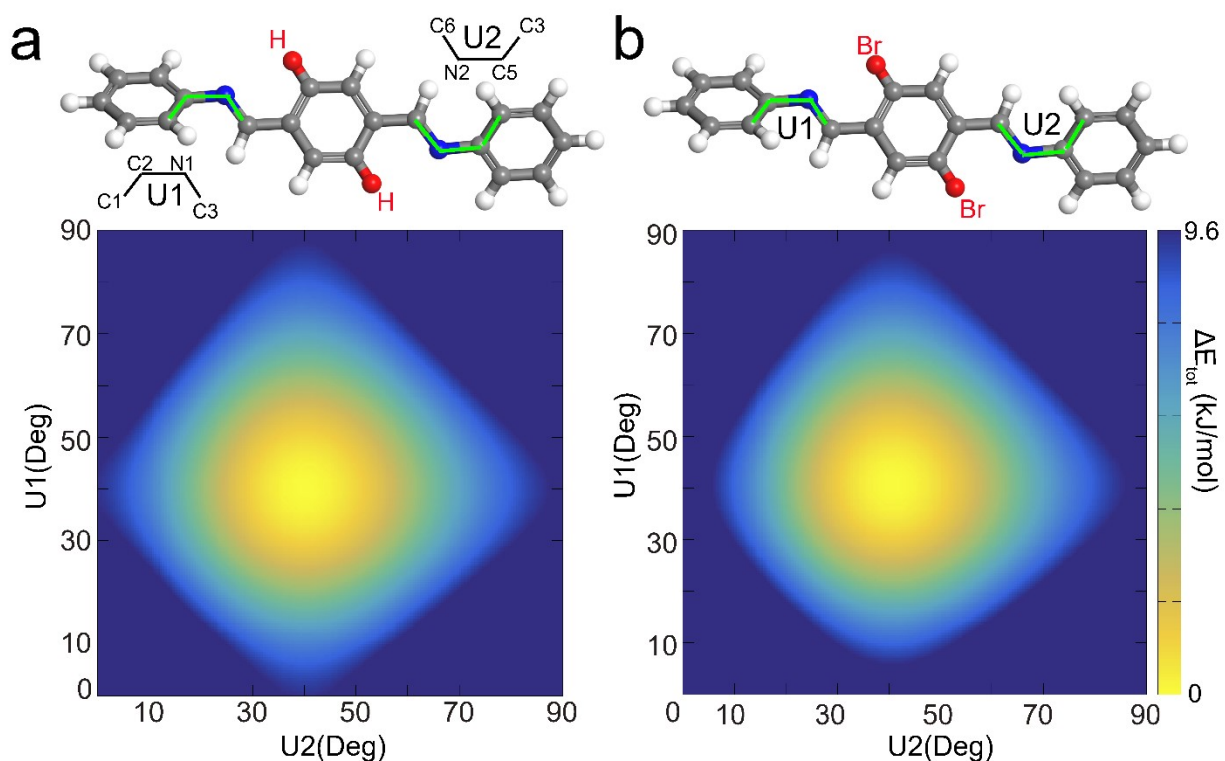


Figure. S58. Energy surface plots for different values of dihedral angles U1 and U2 in the molecular model (a) TAPB-PDA-TAPB unit and (b) TAPB-BrPDA-TAPB unit.

The moieties linked at both sides of  $-C=N-$  bonds have two types of dihedral angles U and Z as shown in Figure. S57A. We first calculated the energy surface as functions of U and Z for the model in Figure. S57A, and the results were shown in Figure. S57B. Observed from the energy surface plot, the lowest conformation energy located at the dihedral angles  $(U, Z) = (\pm 40^\circ, 180^\circ)$ . When Z is fixed, the distortion along U direction from  $-90^\circ$  to  $90^\circ$  resulted in minor energy change. However, when U is fixed, the distortion along Z direction from  $90^\circ$  to  $270^\circ$  result in significant energy change. Therefore, the distortion energy along dihedral angles Z was significantly higher than that along U direction, indicating that Z-direction distortion is not preferred.

### Section 3. Engineering robustness through multivariate approach

#### 3.1. Extra data for TAPB-PDA<sub>x</sub>-C8PDA<sub>y</sub> COFs

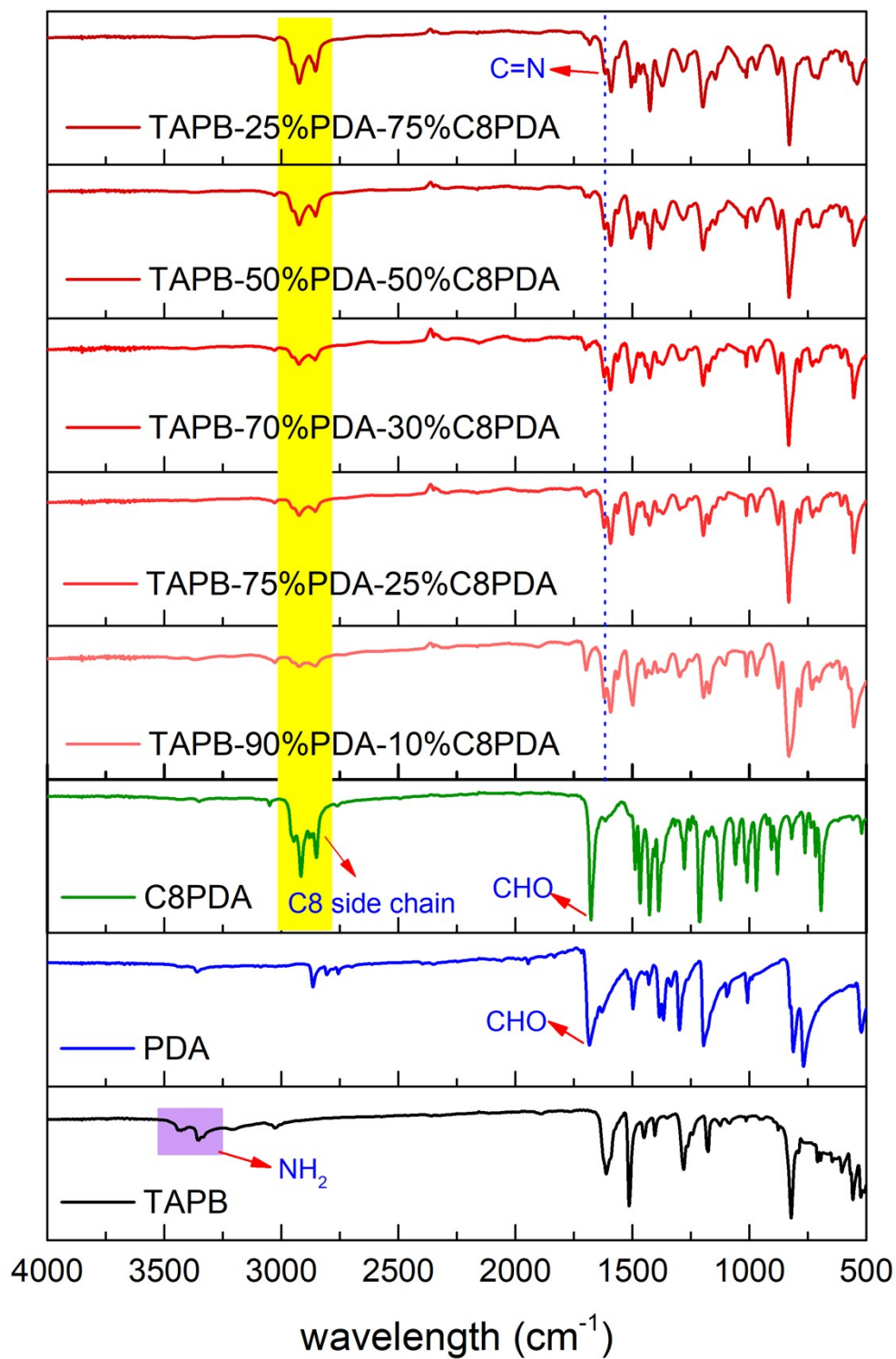


Figure. S59. FTIR spectra for TAPB-PDA<sub>x</sub>-C8PDA<sub>y</sub> COFs after PFH activation.

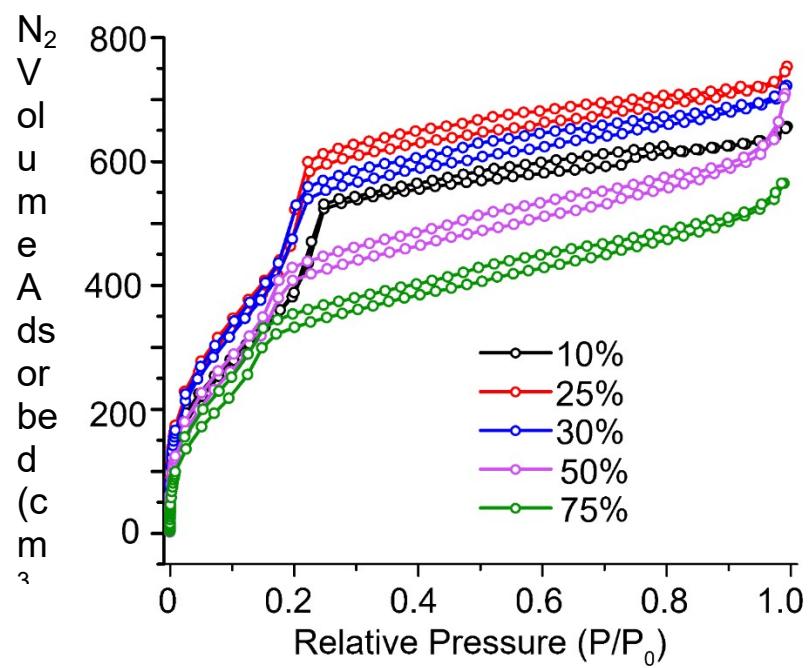


Figure. S60. Nitrogen sorption isotherms for TAPB-PDAX-C8PDAY COFs after PHF activation.

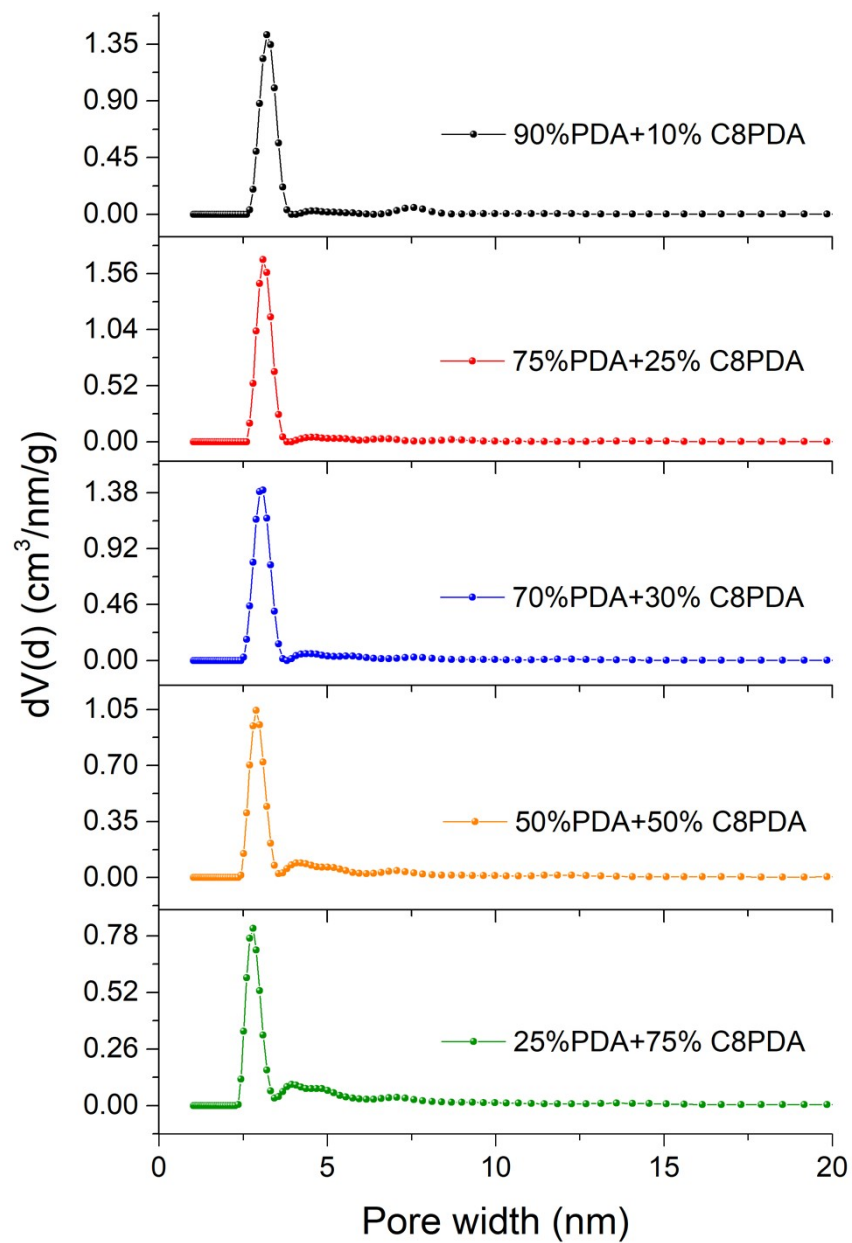


Figure. S61. Pore size distributions of TAPB-PDA<sub>x</sub>-C8PDA<sub>y</sub> COFs after PFH activation calculated using QSDFT model.

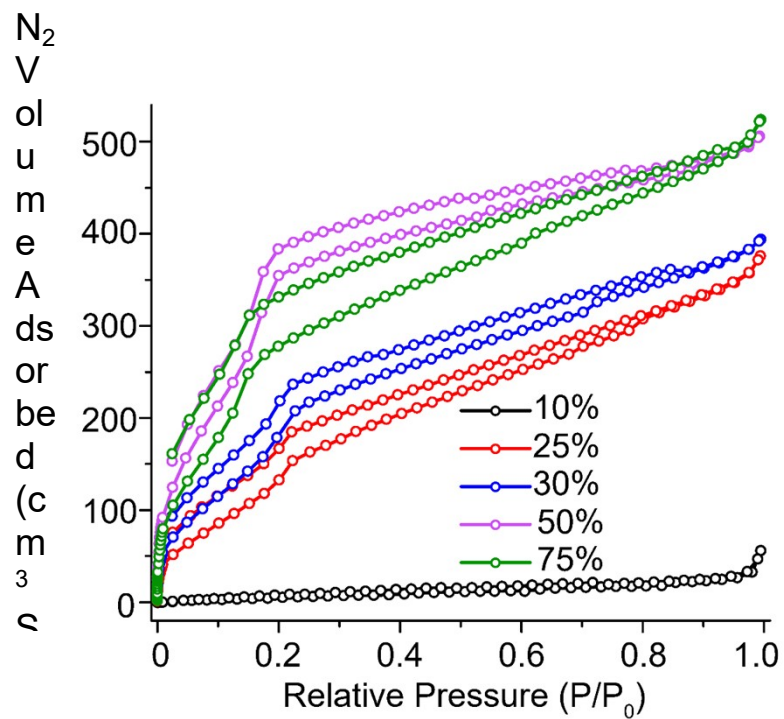


Figure. S62. Nitrogen sorption isotherms for TAPB-PDAX-C8PDAY COFs after THF activation.

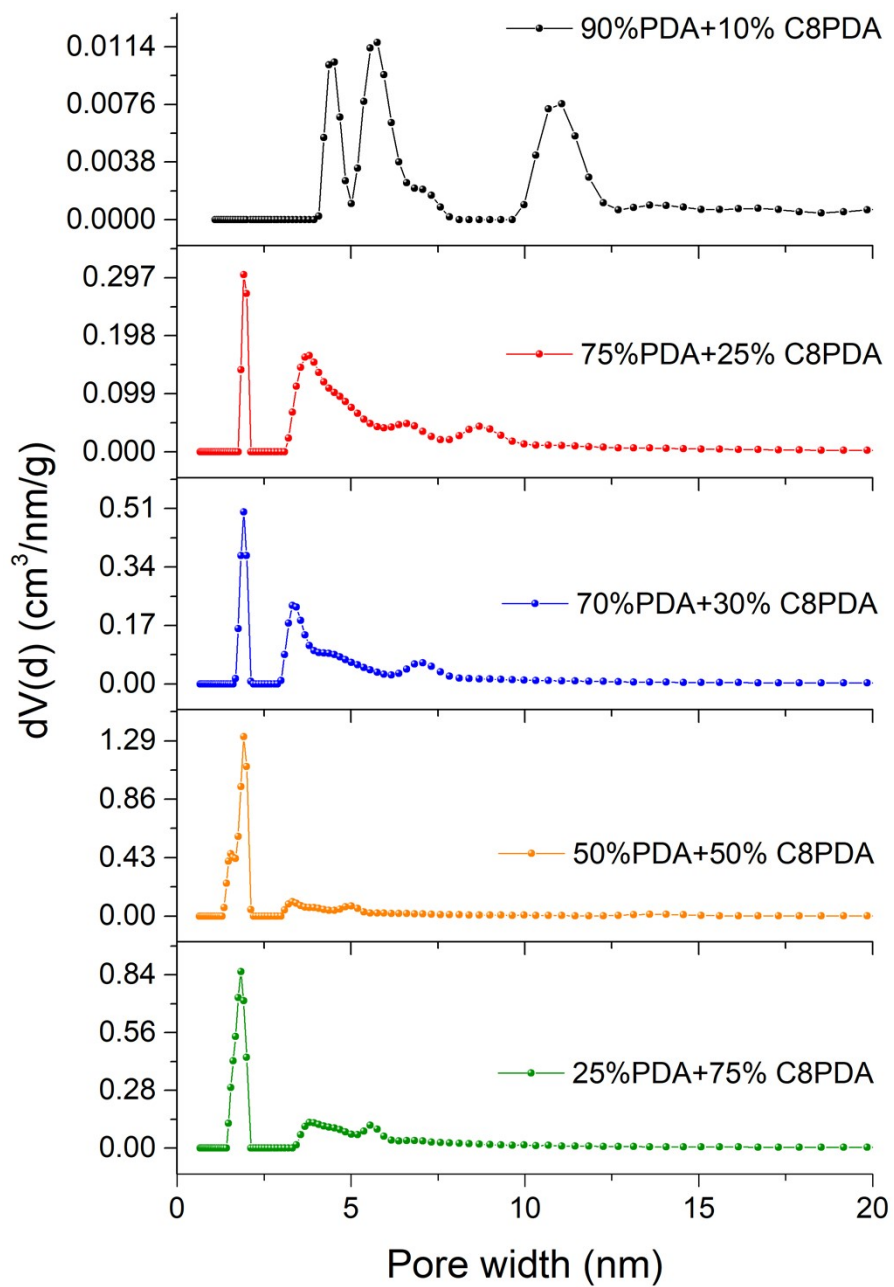


Figure. S63. Pore size distributions of TAPB-PDA<sub>x</sub>-C8PDA<sub>y</sub> COFs after THF activation calculated using QSDFT model.

### 3.2. Extra data for TAPB-PDA<sub>x</sub>-OMePDA<sub>y</sub> COFs

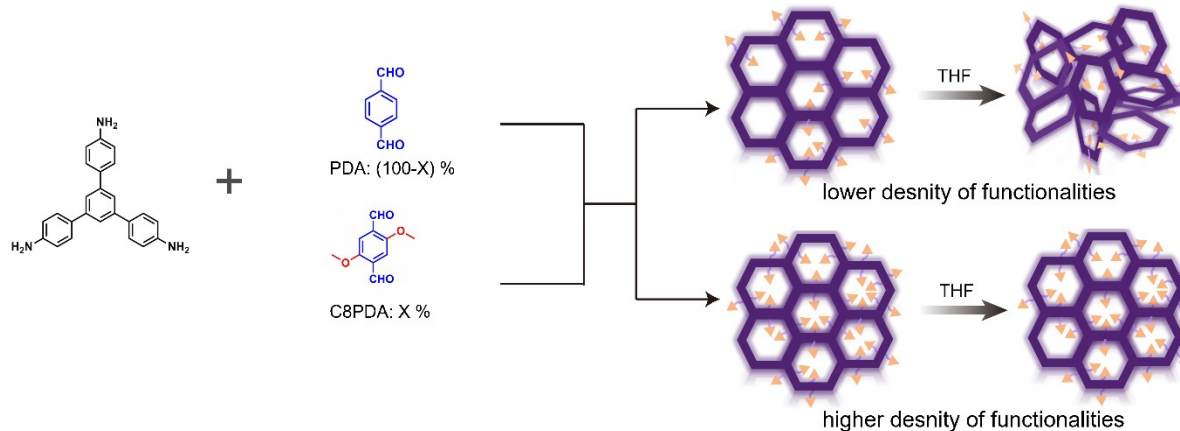


Figure. S64. Reaction scheme and schematic for tailoring COF robustness through systematic variations in pore functionality. The schematic shows that increasing the number of pore functionalities improves robustness.

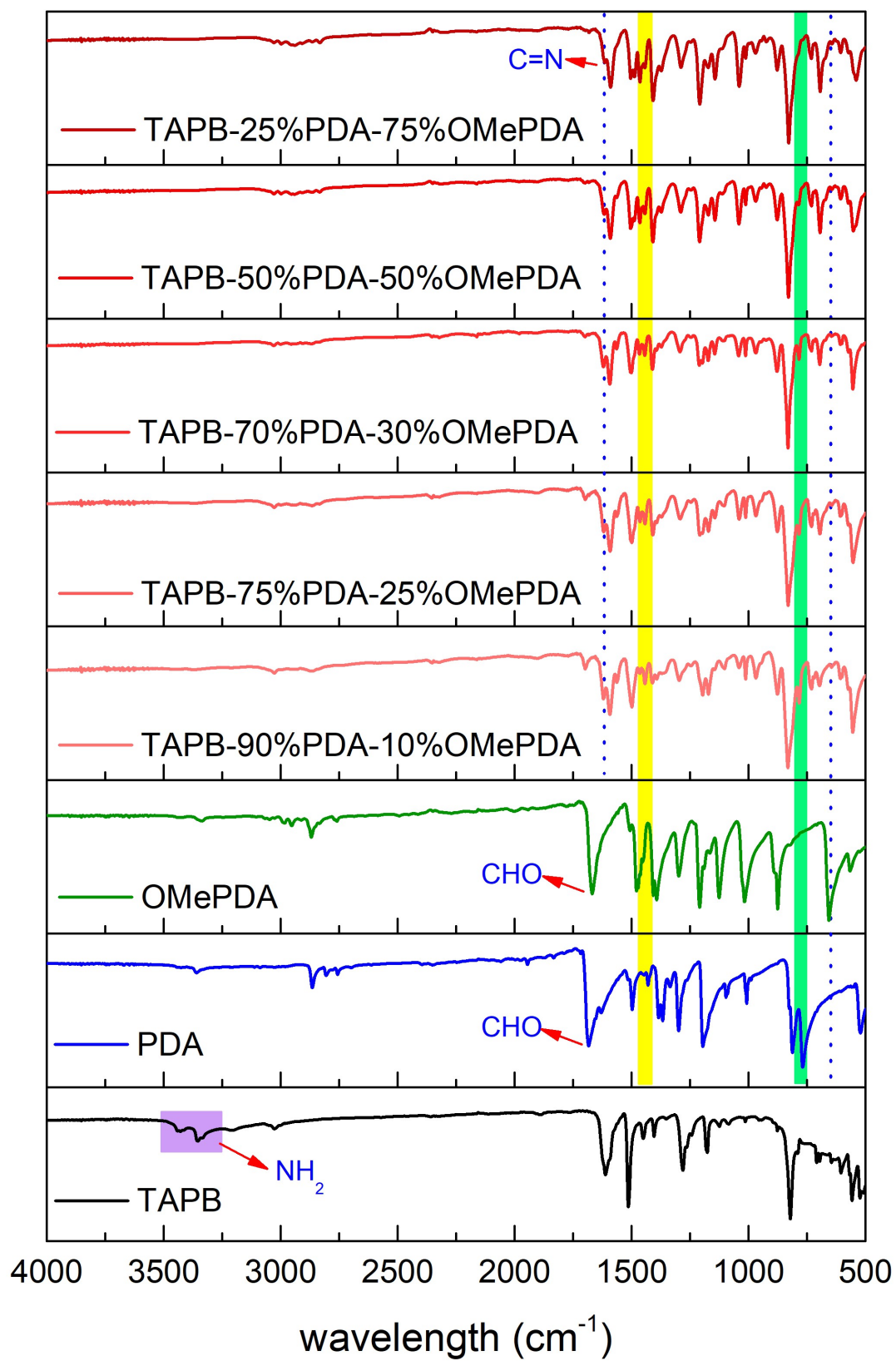


Figure. S65. FTIR spectra for TAPB-PDA<sub>x</sub>-OMePDA<sub>y</sub> COFs.

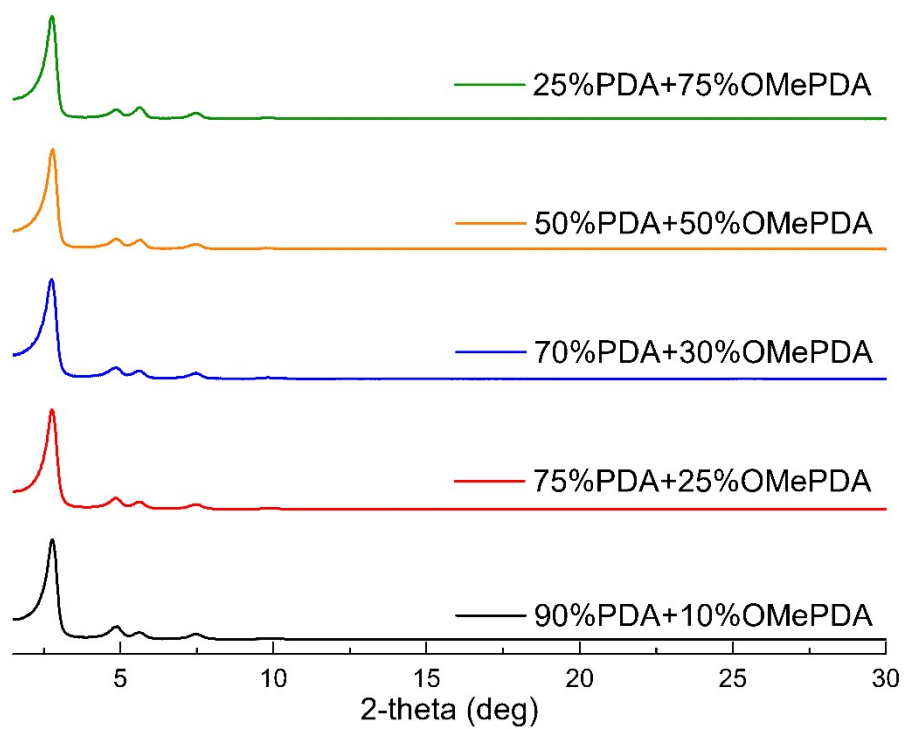


Figure. S66. PXRD patterns for TAPB-PDax-OMePDAY COFs after activation using PFH.

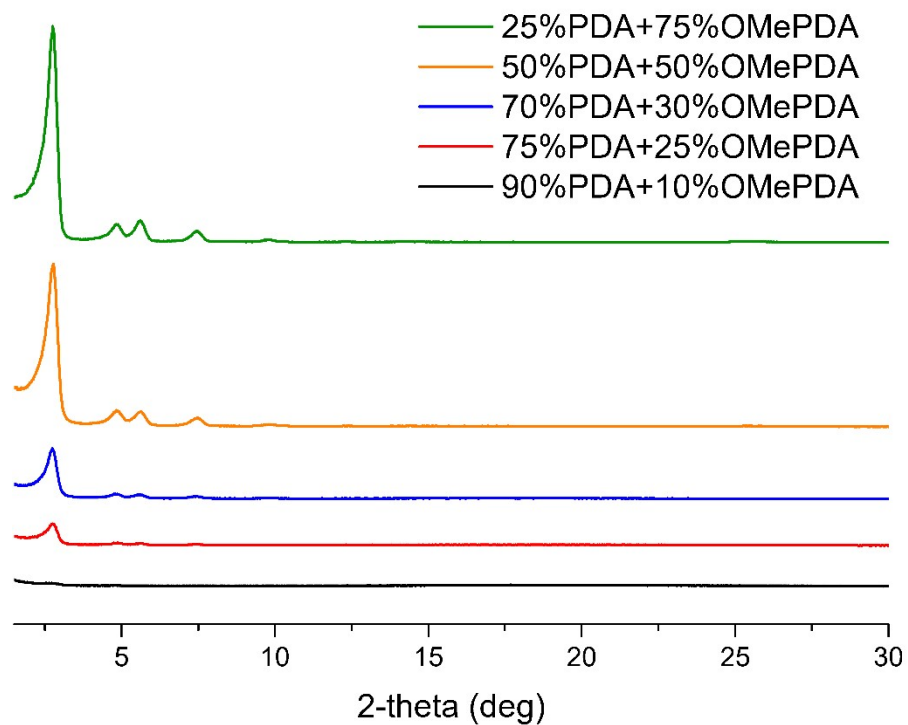


Figure. S67. PXRD patterns for TAPB-PDA<sub>x</sub>-OMePDA<sub>y</sub> COFs after activation using THF.

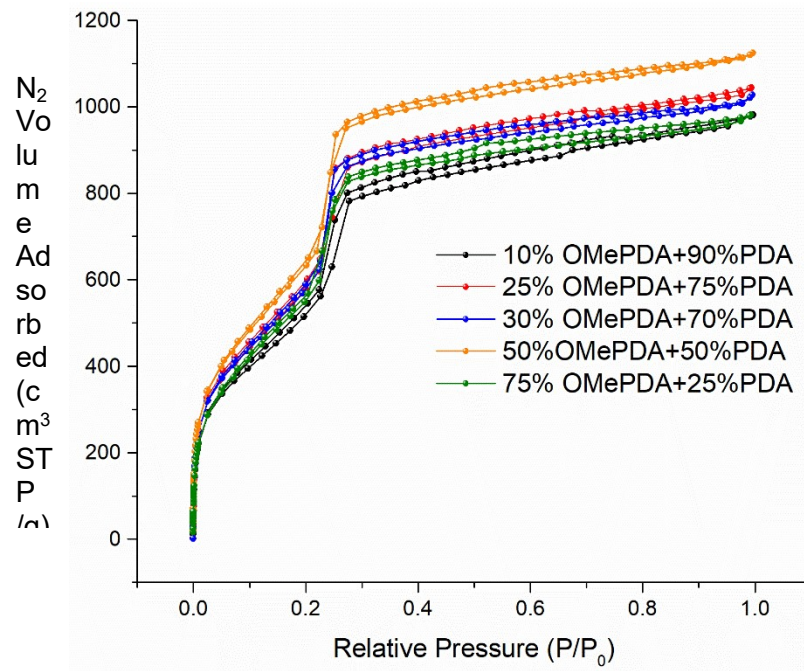


Figure. S68. Nitrogen sorption isotherms for TAPB-PDA<sub>x</sub>-OMePDA<sub>y</sub> COFs after activation using PFH.

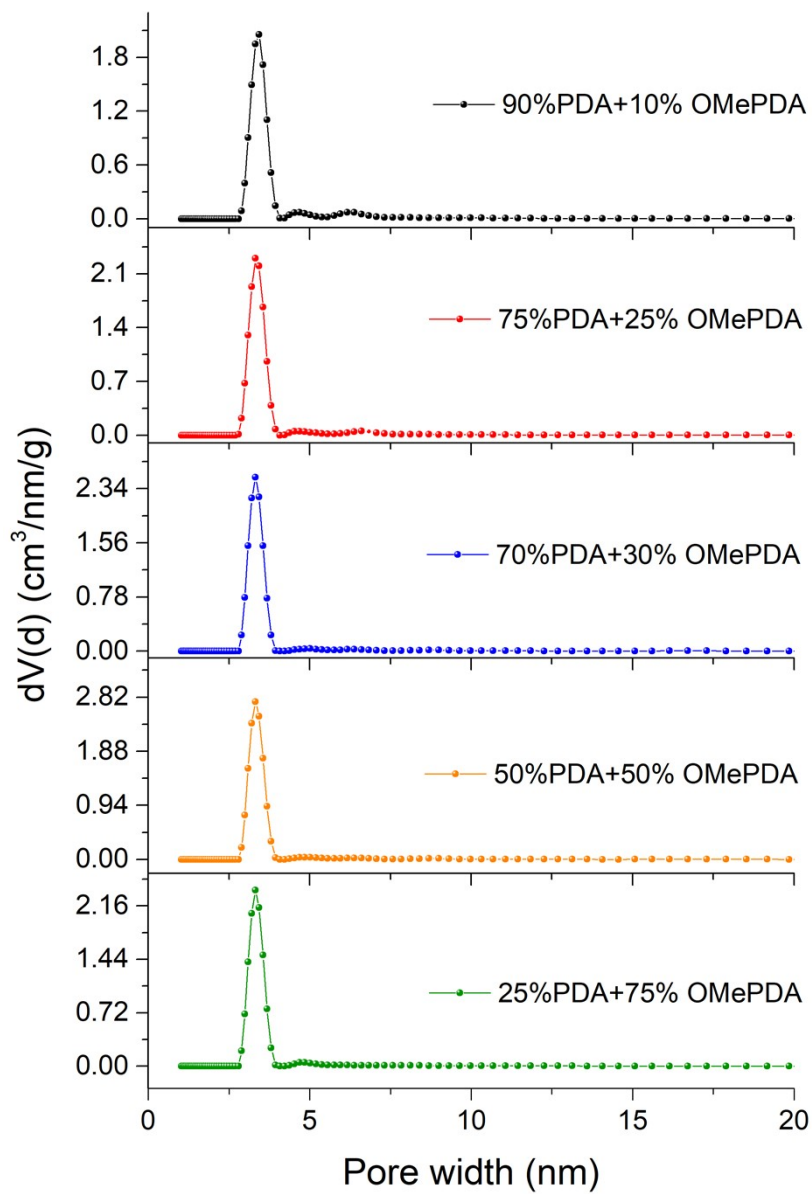


Figure. S69. Pore size distributions of TAPB-PDA<sub>x</sub>-OMePDA<sub>y</sub> COFs after PFH activation calculated using QSDFT model.

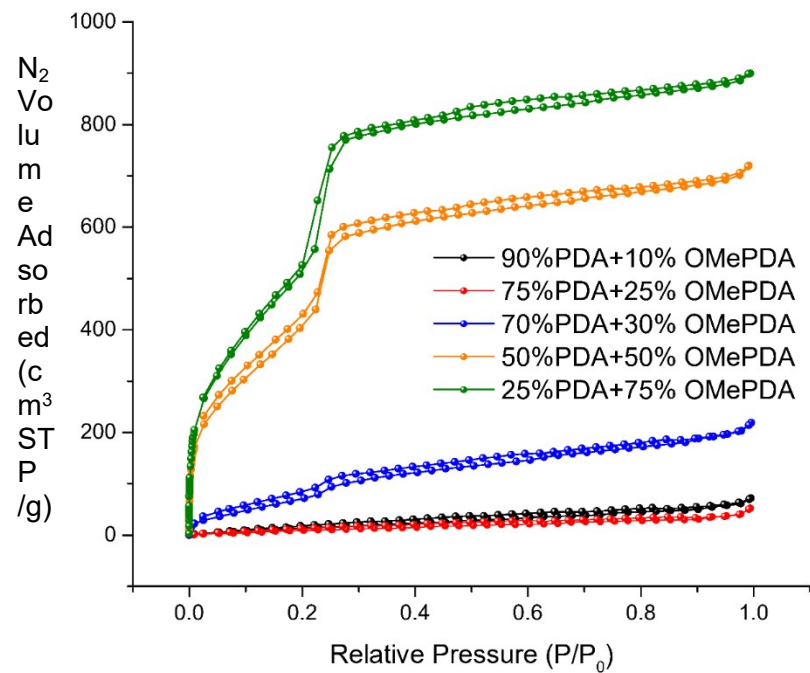


Figure. S70. Nitrogen sorption isotherms for TAPB-PDA<sub>x</sub>-OMePDA<sub>y</sub> COFs after activation using THF.

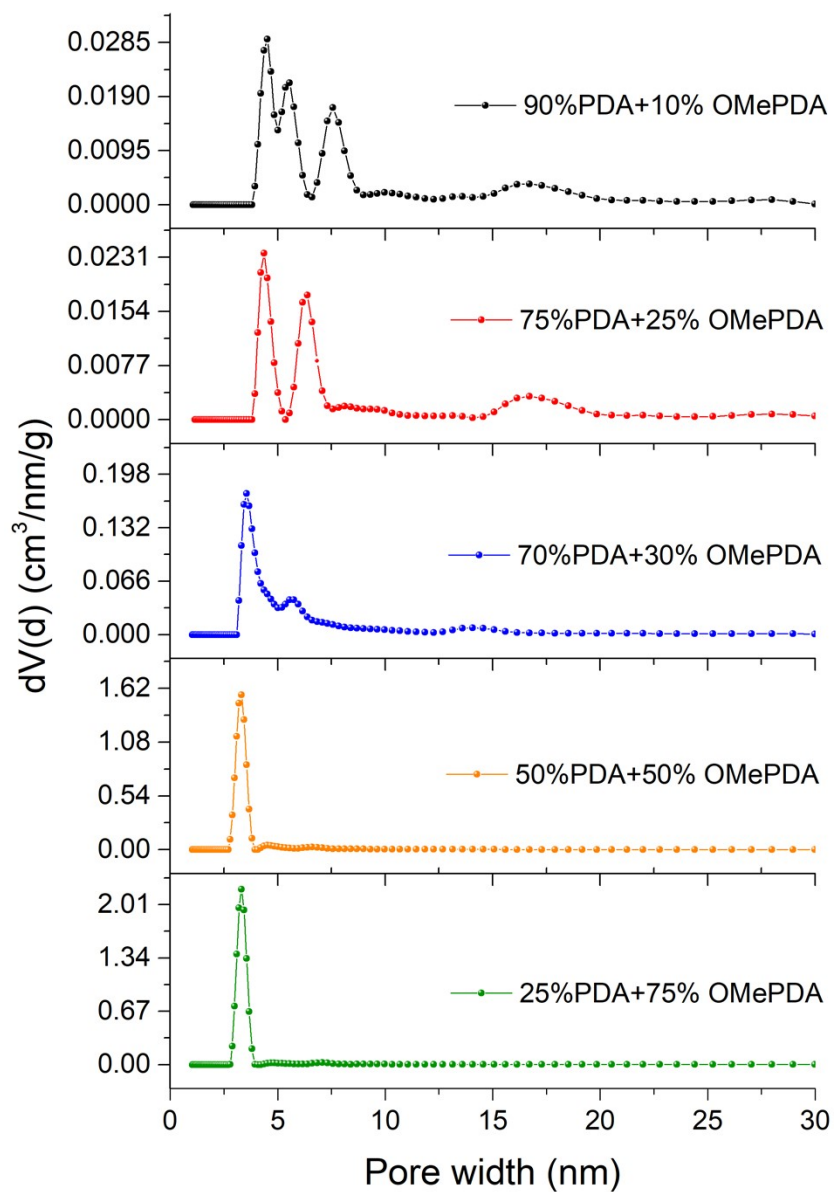


Figure. S71. Pore size distributions of TAPB-PDA<sub>x</sub>-OMePDA<sub>y</sub> COFs after THF activation calculated using QSDFT model.

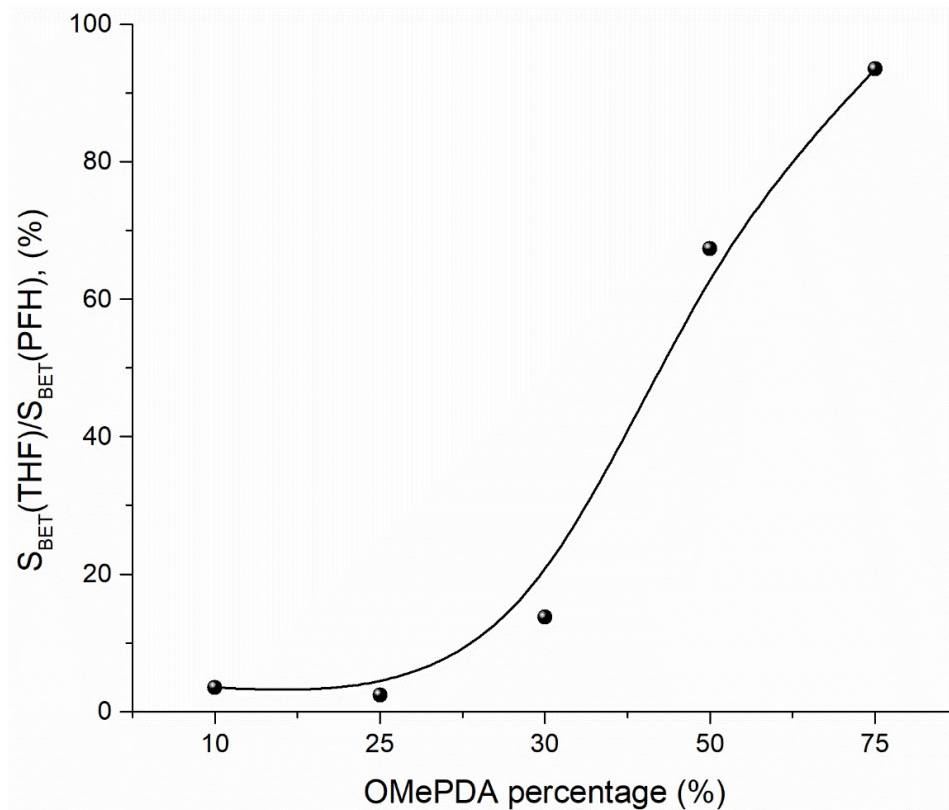


Figure. S72. BET surface area of COFs activated by THF relative to the surface area measured after PFH activation. COFs with a higher methoxyl pore functionality content are more robust, as measured by the percentage of BET surface area retained after THF activation relative to that after PFH activation.

Table S1. Synthesis conditions for each COF

Pore size	Solvents, reaction conditions
TAPB-BTCA	dioxane=1.5 ml; mesitylene=1.5 ml; 6M AcOH=0.3 ml; 120 °C, 3 days
TAPB-TFPA	dioxane/mesitylene/6M AcOH=5:5:1, v/v/v; 120 °C, 3 days
TAPB-TFPB	dioxane/mesitylene/6M AcOH=8:2:1, v/v/v; 120 °C, 3 days
PI-2	o-dichlorobenzene/1-butanol/6M AcOH=19:1:2, v/v/v; 120 °C, 3 days
Pore functionality	
TAPB-FPDA	dioxane/mesitylene/6M AcOH=8:2:1, v/v/v; 120 °C, 3 days
TAPB-OHPDA	dioxane/mesitylene/6M AcOH=8:2:1, v/v/v; 120 °C, 3 days
TAPB-CIPDA	dioxane/mesitylene/6M AcOH=8:2:1, v/v/v; 120 °C, 3 days
TAPB-BrPDA	dioxane/mesitylene/6M AcOH=8:2:1, v/v/v; 120 °C, 3 days
TAPB-OMePDA	dioxane/mesitylene/6M AcOH=8:2:1, v/v/v; 120 °C, 3 days
Pore architecture	
Py-1P	dioxane/mesitylene/6M AcOH=10:20:3, v/v/v; 120 °C, 7 days
Py-OH1P	o-dichlorobenzene/1-butanol/6M AcOH=5:5:2, v/v/v; 120 °C, 3 days
Py-2P	o-dichlorobenzene/1-butanol/6M AcOH=5:5:2, v/v/v; 120 °C, 3 days
Py-OMe3P	o-dichlorobenzene/1-butanol/6M AcOH=19:1:2, v/v/v; 120 °C, 3 days

Table S2. BET surface areas for COFs studied in pore size series after activation using PFH and

THF

COFs	$S_{\text{BET}}(\text{PFH}) \text{ m}^2 \text{ g}^{-1}$	$S_{\text{BET}}(\text{MeOH}) \text{ m}^2 \text{ g}^{-1}$	$S_{\text{BET}}(\text{THF}) \text{ m}^2 \text{ g}^{-1}$
TAPB-BTCA	1022	1001	956
TAPB-TFPA	1125	1140	841
TAPB-TFPB	687	651	108
PI-2	780	215	224
TAPB-PDA	1919	45	30

Table S3. BET surface areas for COFs with different pore functionalities

COFs	$S_{\text{BET}}(\text{PFH})$ $\text{m}^2 \text{g}^{-1}$	$S_{\text{BET}}(\text{MeOH})$ $\text{m}^2 \text{g}^{-1}$	$S_{\text{BET}}(\text{THF})$ $\text{m}^2 \text{g}^{-1}$
TAPB-PDA	1919	45	30
TAPB-FPDA	653	75	55
TAPB-OHPDA	1452	1190	155
TAPB-CIPDA	1996	1952	1873
TAPB-BrPDA	1689	1555	1559
TAPB-OMePDA	2205	2213	2194

Table S4. BET surface areas for COFs with rhombic topology

COFs	$S_{\text{BET}}(\text{PFH}), \text{m}^2 \text{g}^{-1}$	$S_{\text{BET}}(\text{MeOH}), \text{m}^2 \text{g}^{-1}$	$S_{\text{BET}}(\text{THF}), \text{m}^2 \text{g}^{-1}$
Py-OH1P	901	938	763
Py-1P	2598	2321	1504
Py-2P	3312	3121	91
Py-OMe3P	1786	1580	77

Table S5. Fractional atomic coordinates for Py-OMe3P COF.

Py-OMe3P COF			
Atom	x	y	z
N1	-0.35894	-0.38042	2.63619
C2	-0.43782	-0.47476	3.06097
C3	-0.46893	-0.47466	3.27774
C4	-0.48486	-0.45007	3.39447
C5	-0.41846	-0.4495	2.95891
C6	-0.42769	-0.42683	2.79566
C7	-0.40889	-0.40371	2.6943
C8	-0.37979	-0.40315	2.74415
C9	-0.37019	-0.42597	2.89833
C10	-0.38928	-0.44884	3.00653
C11	-0.36413	-0.35701	2.50468
C12	-0.34018	-0.33561	2.4048
C13	-0.31074	-0.34046	2.42846
C14	-0.34692	-0.3099	2.28398
C15	-0.71257	-0.31863	4.67476
C16	-0.70482	-0.29312	4.7887
C17	-0.67514	-0.28903	4.80993
C18	-0.75636	-0.7236	5.14351
C19	-0.77871	-0.74432	5.25482
C20	-0.72787	-0.72913	4.8925
O21	-0.80717	-0.73995	5.51837
C22	-0.81517	-0.71286	5.65747
H23	-0.47433	-0.43019	3.32791
H24	-0.44935	-0.42706	2.74285
H25	-0.41704	-0.38696	2.56782
H26	-0.34791	-0.42571	2.93926
H27	-0.38144	-0.46592	3.13273
H28	-0.38603	-0.3525	2.4681
H29	-0.30496	-0.35999	2.52379
H30	-0.36949	-0.30592	2.26152
H31	-0.73525	-0.32234	4.65483
H32	-0.66919	-0.26943	4.90345
H33	-0.7606	-0.70314	5.25402

H34	-0.81646	-0.69842	5.44359
H35	-0.79873	-0.7052	5.79208
H36	-0.8381	-0.7136	5.86022
C37	-0.57661	-0.5	4.05005
C38	-0.51552	-0.5	3.61296
H39	0.39999	0.5	2.22477

Table S6. Elemental analysis results for TAPB-PDA<sub>x</sub>-C8PDA<sub>y</sub> COFs

Sample	C wt.%	N wt.%	H wt.%
TAPB-PDA <sub>10</sub> -C8PDA <sub>90</sub>	78.2	6.5	4.0
TAPB-PDA <sub>25</sub> -C8PDA <sub>75</sub>	84.5	6.6	5.3
TAPB-PDA <sub>30</sub> -C8PDA <sub>70</sub>	84.0	6.4	5.4
TAPB-PDA <sub>50</sub> -C8PDA <sub>50</sub>	83.1	5.6	6.3
TAPB-PDA <sub>75</sub> -C8PDA <sub>25</sub>	83.1	5.3	6.8

Table S7. BET surface areas for TAPB-PDA<sub>x</sub>-C8PDA<sub>y</sub> COFs after PFH and THF activation.

COFs	90%PDA+ 10%C8PDA	75%PDA+ 25% C8PDA	70%PDA+ 30% C8PDA	50%PDA+ 50% C8PDA	25%PDA+ 75% C8PDA
S <sub>BET</sub> (PFH) (m <sup>2</sup> g <sup>-1</sup> )	1539	1904	1979	1903	1534
S <sub>BET</sub> (THF) (m <sup>2</sup> g <sup>-1</sup> )	28	534	822	1584	1422

Table S8. Elemental analysis results for TAPB-PDA<sub>x</sub>-OMePDA<sub>y</sub> COFs

Sample	C w.t.%	N w.t.%	H w.t.%
TAPB-PDA <sub>10</sub> -OMePDA <sub>90</sub>	85.6	8.0	4.3
TAPB-PDA <sub>25</sub> -OMePDA <sub>75</sub>	81.4	7.8	3.8
TAPB-PDA <sub>30</sub> -OMePDA <sub>70</sub>	83.3	7.8	4.0
TAPB-PDA <sub>50</sub> -OMePDA <sub>50</sub>	81.8	7.4	4.2
TAPB-PDA <sub>75</sub> -OMePDA <sub>25</sub>	80.3	7.0	4.4

Table S9. BET surface areas for TAPB-PDA<sub>x</sub>-OMePDA<sub>y</sub> COFs after PFH and THF activation.

COFs	90%PDA+ 10%OMePDA	75%PDA+ 25%OMePDA	70%PDA+ 30%OMePDA	50%PDA+ 50%OMePDA	25%PDA+ 75%OMePDA
S <sub>BET</sub> (PFH) (m <sup>2</sup> g <sup>-1</sup> )	1956	2197	2170	2391	2173
S <sub>BET</sub> (THF) (m <sup>2</sup> g <sup>-1</sup> )	69	53	298	1611	2031

## SI References

1. G. Kresse, J. Furthmüller, Efficient iterative schemes for ab initio total-energy calculations using a plane-wave basis set. *Physical Review B*. **54**, 11169–11186 (1996).
2. G. Kresse, D. Joubert, From ultrasoft pseudopotentials to the projector augmented-wave method. *Physical Review B*. **59**, 1758–1775 (1999).
3. Gaussian 16, Revision A.03, M. J. Frisch, G. W. Trucks, H. B. Schlegel, G. E. Scuseria, M. A. Robb, J. R. Cheeseman, G. Scalmani, V. Barone, G. A. Petersson, H. Nakatsuji, X. Li, M. Caricato, A. V. Marenich, J. Bloino, B. G. Janesko, R. Gomperts, B. Mennucci, H. P. Hratchian, J. V. Ortiz, A. F. Izmaylov, J. L. Sonnenberg, D. Williams-Young, F. Ding, F. Lipparini, F. Egidi, J. Goings, B. Peng, A. Petrone, T. Henderson, D. Ranasinghe, V. G. Zakrzewski, J. Gao, N. Rega, G. Zheng, W. Liang, M. Hada, M. Ehara, K. Toyota, R. Fukuda, J. Hasegawa, M. Ishida, T. Nakajima, Y. Honda, O. Kitao, H. Nakai, T. Vreven, K. Throssell, J. A. Montgomery, Jr., J. E. Peralta, F. Ogliaro, M. J. Bearpark, J. J. Heyd, E. N. Brothers, K. N. Kudin, V. N. Staroverov, T. A. Keith, R. Kobayashi, J. Normand, K. Raghavachari, A. P. Rendell, J. C. Burant, S. S. Iyengar, J. Tomasi, M. Cossi, J. M. Millam, M. Klene, C. Adamo, R. Cammi, J. W. Ochterski, R. L. Martin, K. Morokuma, O. Farkas, J. B. Foresman, and D. J. Fox, Gaussian, Inc., Wallingford CT, 2016.
4. B. Delley, From molecules to solids with the DMol3 approach. *The Journal of Chemical Physics*. **113**, 7756–7764 (2000).
5. B. Delley, An all-electron numerical method for solving the local density functional for polyatomic molecules. *The Journal of Chemical Physics*. **92**, 508–517 (1990).
6. N. Keller, M. Calik, D. Sharapa, H. R. Soni, P. M. Zehetmaier, S. Rager, F. Auras, A. C. Jakowetz, A. Görling, T. Clark, T. Bein, Enforcing Extended Porphyrin J-Aggregate Stacking in Covalent Organic Frameworks. *Journal of the American Chemical Society*. **140**, 16544–16552 (2018).
7. S. Wan, F. Gándara, A. Asano, H. Furukawa, A. Saeki, S. K. Dey, L. Liao, M. W. Ambrogio, Y. Y. Botros, X. Duan, S. Seki, J. F. Stoddart, O. M. Yaghi, Covalent Organic Frameworks with High Charge Carrier Mobility. *Chemistry of Materials*. **23**, 4094–4097 (2011).